# The climatic significance of Late Ordovician-early Silurian black shales

**A. Pohl[1], Y. Donnadieu[1,2], G. Le Hir[3], and D. Ferreira[4]**

[1]Laboratoire des Sciences du Climat et de l'Environnement, LSCE/IPSL, CEA-CNRS-UVSQ, Université Paris-Saclay, F-91191 Gif-sur-Yvette, France

[2]Aix Marseille Univ, CNRS, IRD, Coll France, CEREGE, Aix-en-Provence, France

[3]IPGP – Institut de Physique du Globe de Paris, Université Paris7-Denis Diderot, 1 rue Jussieu, 75005 Paris, France

[4]Department of Meteorology, University of Reading, Reading, United Kingdom

**Key Points:**

- Up-to-date ocean general circulation model with biogeochemical capabilities (MIT-gcm)
- Investigating the mechanisms responsible for the burial of organic carbon throughout the Ordovician–Silurian boundary
- Simulations suggest a global ocean oxygenation event during the latest Ordovician Hirnantian

---

Corresponding author: A. Pohl, pohl.alexandre@gmail.com

## Abstract

The Ordovician-Silurian transition (~ 455-430 Ma) is characterized by repeated climatic perturbations, concomitant with major changes in the global oceanic redox state best exemplified by the periodic deposition of black shales. The relationship between the climatic evolution and the oceanic redox cycles, however, remains largely debated. Here, using an ocean-atmosphere general circulation model accounting for ocean biogeochemistry (MITgcm), we investigate the mechanisms responsible for the burial of organic carbon immediately before, during and right after the latest Ordovician Hirnantian (445-444 Ma) glacial peak. Our results are compared with recent sedimentological and geochemical data. We show that the late Katian time slice (~ 445 Ma), typified by the deposition of black shales at tropical latitudes, represents an unperturbed oceanic state, with regional organic carbon burial driven by the surface primary productivity. During the Hirnantian, our experiments predict a global oxygenation event, in agreement with the disappearance of the black shales in the sedimentary record. This suggests that deep-water burial of organic matter may not be a tenable triggering factor for the positive carbon excursion reported at that time. Our simulations indicate that the perturbation of the ocean circulation induced by the release of freshwater, in the context of the post-Hirnantian deglaciation, does not sustain over sufficiently long geological periods to cause the Rhuddanian (~ 444 Ma) oceanic anoxic event. Input of nutrients to the ocean, through increased continental weathering and the leaching of newly-exposed glaciogenic sediments, may instead constitute the dominant control on the spread of anoxia in the early Silurian.


## 1 Introduction

For more than 25 million years (~ 455-430 Ma), the Late Ordovician-early Silurian underwent periodic episodes of massive organic matter burial, as testified by the abundant black shale record [*Cramer and Saltzman*, 2007a; *Page et al.*, 2007; *Armstrong et al.*, 2009; *Le Heron et al.*, 2009, 2013; *Melchin et al.*, 2013]. These sedimentary rocks, which include a variety of dark-colored, fine-grained organic-rich lithologies [*Arthur*, 1979; *Trabucho-Alexandre et al.*, 2012], represent perennial organic carbon burial and sequestration in the oceanic sediments under oxygen-depleted depositional settings. Given the amplitude of these events, some authors [*Page et al.*, 2007; *Melchin et al.*, 2013] propose that they may have been comparable to the widely documented Mesozoic Oceanic Anoxic Events [OAEs, *Schlanger and Jenkyns*, 2007; *Jenkyns*, 2010], although the significantly longer duration of the early Paleozoic OAEs remains difficult to explain (2-3 Myr at least, see *Page et al.*, 2007 and *Melchin et al.*, 2013 , compared to 600 kyr to 900 kyr for the Cretaceous OAE2, see *Sageman et al.*, 2006 ) and the concomitant deposition of anoxic sediments in the deep ocean debated due to the non-preservation of pre-Mesozoic ocean bottom sediments.

Despite a comprehensive analysis of combined sedimentological and geochemical data [e.g., *Finney et al.*, 1999; *Brenchley et al.*, 2003; *Kump et al.*, 1999; *Trotter et al.*, 2008; *Hammarlund et al.*, 2012; *Melchin et al.*, 2013], major uncertainties persist about the physical mechanisms that drove the Ordovician-Silurian oxic-anoxic cycles and associated periods of black shale deposition, thus hampering our overall understanding of the coupled Early Paleozoic climate changes and faunal turnovers [*Harper et al.*, 2013a; *Trotter et al.*, 2016]. The relationships between global climate and oceanic redox conditions, in particular, remain largely debated.

Several conceptual models of oceanic cycles were proposed in the past to explain the changes in lithology, biology and carbon isotope stratigraphy during the early Silurian [*Jeppsson*, 1990; *Bickert et al.*, 1997; *Cramer and Saltzman*, 2005]. The seminal model of *Jeppsson* [1990], in particular, suggests the alternation between 2 oceanic states. Black shales form in both of theses climatic modes, but the locus of organic burial differs. *Primo* (P) episodes correspond to cold periods. The ocean bottom is intensively ventilated by cold, oxygenated water masses originating from the zones of deep convection situated at polar latitudes. As a consequence the deep ocean is devoid of black shales. At tropical latitudes, the weathering of the extended Ordovician shelf platforms exposed during the sea-level lowstand promotes the delivery of nutrients to the ocean, fueling the primary productivity and inducing the deposition of black shales on the shelf. Conversely, the warmer climate prevailing during the *Secundo* (S) episodes promotes the stratification of the ocean. The ventilation of the ocean interior is reduced. The ocean bottom is depleted in dissolved oxygen and organic carbon is buried at depth. At low-latitudes, arid conditions prevail. The flux of detrital sediments – and thus nutrients – to the ocean is reduced and the shelf platforms experience extensive reef growth.

The P-S model stimulated vigorous scientific discussion [*Cramer and Saltzman*, 2005, 2007a,b; *Loydell*, 2007, 2008; *Trotter et al.*, 2016; *Munnecke et al.*, 2010]. Nevertheless, several published studies suggest that the proposed alternation between P and S episodes does not satisfactorily capture the lithological and geochemical changes documented in the sedimentary record [*Kaljo et al.*, 2003; *Johnson*, 2006; *Trotter et al.*, 2016]. In addition, the previous conceptual models do not permit any spatialized investigation of the redox state of the ocean. Above all, they are not grounded in physical paleoceanography, which remains highly speculative in the Early Paleozoic [*Servais et al.*, 2014].

Here, we apply an up-to-date ocean general circulation model to study the coupling between climate and ocean biogeochemistry in the Early Paleozoic. Building on the comprehensive Late Ordovician-early Silurian black shale occurrence compilation of *Melchin et al.* [2013], we investigate geological events able to explain the deposition of black shales and propose driving mechanisms for the redox changes reported immediately before, during and right after the latest Ordovician Hirnantian, from the late Katian to early Silurian Rhuddanian. This time interval includes the Hirnantian glacial maximum [*Denis et al.*, 2007; *Ghienne et al.*, 2007; *Loi et al.*, 2010] and associated mass extinction event [*Sheehan*, 2001; *Rasmussen and Harper*, 2011; *Harper et al.*, 2013b,a], and ultimately constitutes an outstanding window into the coupled climatic, paleoceanographic and biotic perturbations reported for the remainder of the Early Paleozoic Ice Age [*Page et al.*, 2007; *Trotter et al.*, 2016; *Vandenbroucke et al.*, 2015].

Following a description of our experimental setup (Sect. 2), we run our model under a large range of external forcing levels in order to simulate the various climatic conditions reported throughout the studied period of time (Sect. 3). Then, we use these climatic results to investigate the mechanisms driving the patterns of marine biogeochemistry reported by *Melchin et al.* [2013] in each of their three studied time slices: *(i)* the late Katian (Sect. 4); *(ii)* the mid-Hirnantian (Sect. 5); and *(iii)* the early Silurian Rhuddanian (Sect. 6). In the $7^{th}$ section, we discuss the limitations and simplifications associated with our modeling setup and identify future research targets. Finally, we summarize our key findings (Sect. 8).

# 2 Methods

## 2.1 Model description

### *2.1.1 Ocean, sea ice, atmosphere and land*

We use a global ocean-atmosphere coupled setup of the MITgcm. Isomorphisms between the equations that govern the atmosphere and the ocean are exploited to allow a single hydrodynamical core to simulate both fluids [*Marshall et al.*, 2004]. The oceanic and the atmospheric components use the same horizontal model grid, greatly simplifying their coupling. We adopt the conformally expanded spherical cube [*Adcroft et al.*, 2004], with 32 x 32 points per face (CS32) – providing a mean equatorial resolution of 2.8° x 2.8°. The cubed sphere provides a relatively even grid spacing throughout the domain and avoids polar singularities, thus allowing accurate simulation of the polar regions. This is especially appropriate to investigate the ocean circulation during the Ordovician, when the Northern Hemisphere was 95 % oceanic with no continental masses present beyond the mid-latitudes. The oceanic component of the model is a state-of-the-art ocean general circulation model (OGCM) rooted in the incompressible, Boussinesq form of the Navier-Stokes equations [*Marshall et al.*, 1997a,b]. Here we use an hydrostatic, implicit free-surface, partial step topography [*Adcroft et al.*, 1997] formulation of the model to simulate the global ocean domain. 28 layers are defined vertically, the thickness of which gradually increases from 10 m at the ocean surface to 1300 m at the bottom, with 18 levels defining the upper 1000 m of the water column. Effects of mesoscale eddies are parametrized as an advective process [*Gent and McWilliams*, 1990] and an isopycnal diffusion [*Redi*, 1982]. The nonlocal K-Profile Parameterization (KPP) scheme of *Large et al.* [1994] accounts for vertical mixing processes in the ocean's surface boundary layer and the interior. Sea ice is simulated using a thermodynamic sea-ice model based on the 3-layer enthalpy-conserving scheme of *Winton* [2000]. Sea ice forms when the ocean temperature falls below the salinity dependent freezing point. The physics of the atmospheric component is based on SPEEDY (Simplified Parametrizations, primitivE-Equation DYnamics, *Molteni*, 2003 ). The latter comprises a four-band longwave radiation scheme (one for the atmospheric "window", a $CO_2$ band with transmissivity tuned to the present-day atmospheric partial pressure of $CO_2$ ($pCO_2$) and the other two bands for the spectral regions of absorption by water vapor), a parametrization of moist convection, diagnostic clouds, and a boundary layer scheme. In the vertical dimension, SPEEDY uses 5 levels. The top and bottom layers respectively represent the stratosphere and the planetary boundary layer. The layers in between account for the free troposphere. SPEEDY has been shown to require at least one order of magnitude less computation time that contemporary state-of-the-art atmospheric GCMs, while providing realistic climate results [*Molteni*, 2003]. Our configuration of the MITgcm also includes a simple, 2-layer land model. No explicit river model is included: the amount of water that exceeds the field capacity of the soil in a given grid point is directly transferred to the ocean following a prescribed mapping. No flux corrections are applied in any of our experiments. The resulting coupled model can be integrated for ~ 100 years in 1 day of dedicated computer time. Relatively similar configurations of the MITgcm were used in the past [*Marshall et al.*, 2007; *Enderton and Marshall*, 2009; *Ferreira et al.*, 2010, 2011; *Brunetti et al.*, 2015], including for paleoceanographic purposes [*Brunetti et al.*, 2015]. A comprehensive description of the coupled model is provided by *Enderton* [2009].

#### *2.1.2 Marine biogeochemistry*

The biogeochemistry model included in the present configuration of the MITgcm explicitly accounts for oxygen concentration and primary productivity in the ocean. Following Michaelis-Menten kinetics, and similar to *McKinley et al.* [2004], the net marine primary productivity (NPP) is computed as a function of available photosynthetically active radiation (PAR) and phosphate concentration ($PO_4$),

$$NPP = \alpha \frac{PAR}{PAR + K_{PAR}} \frac{PO_4}{PO_4 + K_{PO_4}} \quad (1)$$

where $\alpha = 2 \text{ x } 10^{-3}$ mol.m$^{-3}$.yr$^{-1}$ is the maximum community productivity, $K_{PAR} = 30$ W.m$^{-2}$ the half saturation light constant, and $K_{PO_4} = 5 \text{ x } 10^{-4}$ mol.m$^{-3}$ the half saturation phosphate constant. Two thirds of the biological production remains suspended in the water column as dissolved organic phosphorus (DOP), which remineralizes back to phosphate following an *e*-folding time scale of 6 months [*Yamanaka and Tajika*, 1997]. The remainder of the biological production sinks to depth as particulate organic phosphorus (POP) and remineralizes according to the empirical power law of *Martin et al.* [1987]. The oceanic residence time of phosphate is estimated between 10 and 40 kyrs [*Ruttenberg*, 1993; *Wallmann*, 2003], much longer than the oceanic turnover time scale. The globally-averaged oceanic phosphate concentration is therefore fixed in the model, riverine and atmospheric sources are not represented, and sedimentation is not allowed [*Dutkiewicz et al.*, 2005]. Phosphate is consumed to fuel the marine primary productivity in the photic zone, regenerated by remineralization in the water column and ultimately advected-diffused by the global ocean circulation back to the ocean surface in upwelling zones. In the present set-up, phosphate constitutes the single limiting nutrient. Iron is known to significantly constrain primary productivity as well [e.g., *Falkowski*, 2012]. It is essentially supplied to the ocean through atmospheric deposition of mineral dust originating from deserts. Present-day iron dust emissions and flux, however, remain difficult to quantify [e.g., *Bryant*, 2013]. Reconstructing their Early Paleozoic counterparts is challenging, notably implying major assumptions on the land-surface typology. Although our biogeochemistry model does have the provision for explicitly representing cycling of iron, we therefore choose not to consider iron fertilization in the present study. Oxygen is exchanged at the ocean-atmosphere interface following *Garcia and Gordon* [1992] and redistributed within the ocean using the velocity and diffusivity fields provided by the general circulation model. The fate of $O_2$, i.e., transformation to and from organic form, is also tied to that of phosphorus through fixed Redfield stoichiometry. The PAR is defined at the surface of the ocean as the fraction of the incident shortwave radiation that is photosynthetically available. It is then attenuated as it travels through the water column assuming a uniform extinction coefficient. The shortwave radiation is provided by the atmospheric component of our coupled climate model. Similar configurations of the biogeochemistry model were used in the past [e.g., *Friis et al.*, 2006, 2007].

### 2.2 Boundary and initial conditions

Because the geological events under study occurred over a duration that is lower than the temporal resolution of current paleogeographical reconstructions, we use a single continental configuration to simulate climate throughout the whole Ordovician–Silurian boundary. We use the Late Ordovician paleogeography from *Torsvik and Cocks* [2009]. The topography and bathymetry are reconstructed based on studies for Gondwana [*Torsvik and Cocks*, 2013], Laurentia [*Cocks and Torsvik*, 2011], Baltica [*Cocks and Torsvik*, 2005], Siberia [*Cocks and Torsvik*, 2007] and for modern Asia [*Cocks and Torsvik*, 2013]. Because the location of ocean ridges is highly speculative in the Ordovician, they are not included in our reconstruction (i.e., we prescribe a flat bottom). The resulting map (Fig. 1), given in input to the model, is identical to the one used by *Pohl et al.* [2016a, their Fig. 2a]. Because vegetation was restricted to non-vascular plants during the Ordovician [*Steemans et al.*, 2009; *Rubinstein et al.*, 2010], the spatial cover of which is difficult to estimate and largely debated [e.g., *Porada et al.*, 2016; *Heckman et al.*, 2001; *Edwards et al.*, 2015], we follow previous studies [*Nardin et al.*, 2011; *Pohl et al.*, 2014, 2016a,b] and impose a rocky desert on continents (prescribed ground albedo of 0.24, which is modified by snow if present). The orbital configuration is defined with an eccentricity of 0° and an obliquity of 23.45°. The same initial conditions are used in all simulations. The temperature distribution is defined by a theoretical latitudinal temperature gradient, characterized by equatorial and polar ocean surface temperatures of respectively 35 °C and 6 °C, and an ocean bottom initial potential temperature of 3 °C. Ocean is therefore sea-ice free at the beginning of each simulation. A uniform initial salinity of 35 psu (practical salinity units) is imposed over the whole domain. Phosphate and oxygen in the ocean are initialized with present-day depth profiles and DOP is null at the beginning of the simulation. Reconstructions of the Ordovician atmospheric partial pressure of oxygen ($pO_2$) lead to scattered values. *Bergman et al.* [2004] and *Berner* [2006, 2009], using models of biogeochemical cycling, propose values between respectively 0.2 to 0.6, and 0.72 to 0.95 times the present-day level. *Algeo and Ingall* [2007] estimate, by inversion of the Phanerozoic $C_{org}$:P curve, that the Ordovician $pO_2$ was between 0.61 and 0.8 times the current level. Given the large uncertainty in these reconstructions, the atmospheric oxygen partial pressure is kept to its present-day level in the model, and sensitivity tests are conducted for $pO_2$ values ranging between 0.2 and 0.8 times the current value in order to cover the large uncertainties in estimates for the Ordovician. It is noteworthy that in those tests, the changes in $pO_2$ only affect the ocean-atmosphere gas exchange. They do not alter the radiative fluxes as proposed in the recent study by *Poulsen et al.* [2015]. Our coupled ocean-atmosphere-sea-ice-land-surface model (see Sect. 2.1.1) is first run until deep-ocean equilibrium is reached ($\geq$ 2000 years). It is subsequently restarted with the biogeochemistry module (Sect. 2.1.2) for at least 550 additional years (1550 for the sensitivity tests using a reduced $pO_2$, since the initial (present-day) oxygen concentration significantly differs from the equilibrium state in these runs), the last 50 years of which are used to build the climatology files used for analysis (Fig. S1).

## 3 Climatic simulations

Here we simulate various climate states (Sect. 3.1), and subsequently select the model outputs that best reflect the climatic conditions prevailing during each of the three time slices used in the black shale compilation of *Melchin et al.* [2013]: the late Katian, the mid-Hirnantian and the early Silurian Rhuddanian (Sect. 3.2).

### 3.1 Model results

The atmospheric component of our model, SPEEDY, does not account for varying $pCO_2$ levels. The radiative code is parametrized to reproduce present-day-like greenhouse gas concentration (see Sect. 2.1.1). The simulation of different climatic conditions is thus achieved by varying the solar forcing in the model [e.g., *Ferreira et al.*, 2011]. Results are displayed in Fig. 2. Simulated tropical sea-surface temperatures (SSTs) linearly decrease

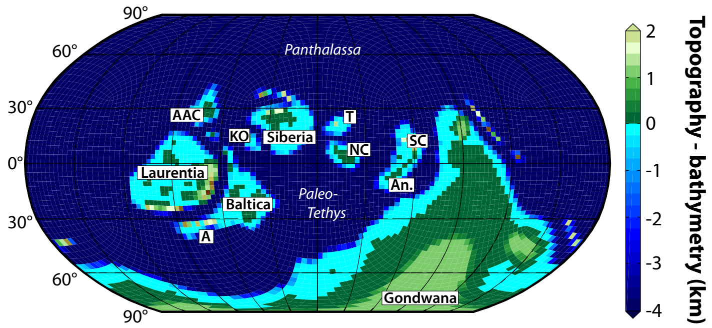


**Figure 1.** Late Ordovician-early Silurian continental reconstruction interpolated on the MITgcm cubed-sphere grid: *AAC: Arctic Alaska-Chukotka*; *KO: Kolyma-Omolon*; *A: Avalonia*; *T: Tarim*; *NC: North China*; *SC: South China*; *An.: Annamia*. Ocean names are in italic.

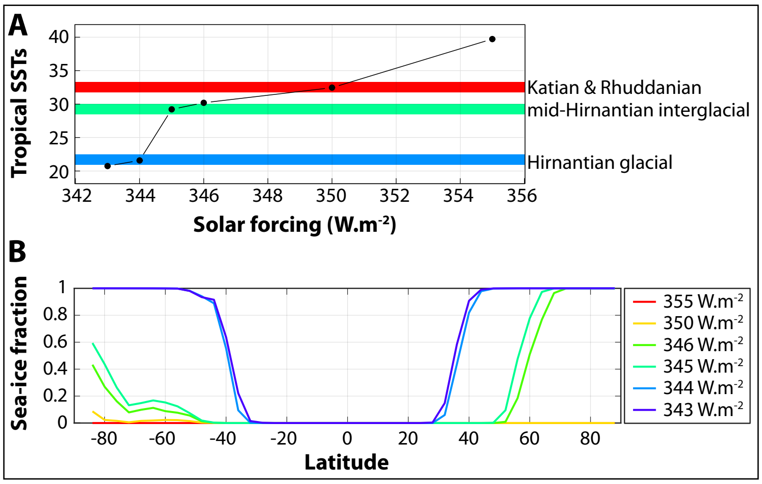


**Figure 2.** Climate results. **(A)**: Mean annual tropical (30° S - 30° N) sea-surface temperatures as a function of the solar forcing level. We here represent the tropical sea-surface temperatures (SSTs), instead of the global surface air temperatures, because Ordovician and Silurian isotopic data are gathered in locations situated at low paleolatitudes. As a consequence they exclusively report variations in tropical SSTs, which thus constitute the most straightforward variable for any model-data comparison [e.g., *Trotter et al.*, 2008; *Finnegan et al.*, 2011]. The colored strips identify the simulations selected throughout this study to investigate the mechanisms governing the deposition of black shales in the 3 time slices documented by *Melchin et al.* [2013]: the late Katian (red), the mid-Hirnantian (green) and the early Rhuddanian (red as well). The Hirnantian glacial state is shown for comparison (blue), but the associated model run is not analyzed in detail in this study. Please note that the colors of the strips correspond to the colors of the lines drawn in subplot **B**. **(B)**: Mean annual latitudinal sea-ice fraction simulated at various solar forcing levels.

with the external forcing level, except between 345 W.m$^{-2}$ and 344 W.m$^{-2}$. At this point, a decrease of 1 W.m$^{-2}$ induces a large drop in tropical SST of 7.6 °C (Fig 2A).

*Pohl et al.* [2014] studied the response of the Ordovician climate system to a decrease in $p$CO$_2$. They demonstrated, using the FOAM climate model [*Jacob*, 1997] and *Blakey*'s [2016] Late Ordovician continental reconstruction, that there is a radiative forcing level (~ 2240 ppm CO$_2$) beyond which Ordovician climate suddenly shifts from a warm state with limited sea-ice extent in the Northern Hemisphere, to a much colder state characterized by the sudden extension of the sea ice to the mid-to-tropical latitudes. Building on previous work investigating the presence of multiple equilibria in aquaplanets [*Rose and Marshall*, 2009; *Ferreira et al.*, 2011], they demonstrated that this climatic instability results from the absence of meridional continental boundaries in the Ordovician Northern Hemisphere. These conditions limit the ocean heat transport to the pole and facilitate the growth of large sea-ice caps. In our study, a similar climatic behavior is obtained. The large cooling simulated between 345 W.m$^{-2}$ and 344 W.m$^{-2}$ is due to the ice-albedo positive feedback associated with the spread of sea ice [Fig. 2B, see *Pohl et al.*, 2014].

### 3.2 Simulating Katian, mid-Hirnantian and early Silurian climate

Over the last decade, prominent insights into the Ordovician-Silurian climatic fluctuations were independently provided by *Trotter et al.* [2008, 2016] and *Finnegan et al.* [2011]. Based respectively on tropical $\delta^{18}O_{apatite}$ and $\Delta^{47}CO_2$ data, they reconstructed temperature trends similar to the $\delta^{18}O_{brach}$- and $\delta^{18}O_{bulk}$-derived SSTs published a decade prior [*Long*, 1993; *Brenchley et al.*, 1994, 1995, 2003], except that the SST values calculated from these new proxy data fall within an acceptable modern-like SST range, significantly contrasting with the unlikely previous ocean temperature estimates of up to ~ 70 °C. *Trotter et al.* [2008] and *Finnegan et al.* [2011] notably demonstrated a sudden, sharp drop in tropical SSTs by ~ 7 °C during the latest Ordovician Hirnantian (445-444 Ma). They also suggested that Ordovician climate was relatively warm before the Hirnantian, with Katian (~ 450 Ma) tropical SSTs ranging between ~ 30 °C [*Trotter et al.*, 2008] and 35 °C [*Finnegan et al.*, 2011]. Among the various climate states simulated in this study (see Fig. 2), the simulation with a solar forcing of 350 W.m$^{-2}$ is characterized by a mean tropical SST of 32.5 °C. In the following, we consider this simulation as representative of the Katian climate state documented by most recent studies [*Trotter et al.*, 2008; *Finnegan et al.*, 2011, Fig. 2A].

Following the relatively warm late Katian period, the latest Ordovician Hirnantian (445-444 Ma) glacial peak is typified by a sudden global climate cooling [*Trotter et al.*, 2008; *Finnegan et al.*, 2011] and the growth of a continental-scale ice-sheet over the South Pole [*Denis et al.*, 2007; *Ghienne et al.*, 2007; *Le Heron and Craig*, 2008; *Loi et al.*, 2010]. During the mid-Hirnantian [upper *extraordinarius*-lower *persculptus* Zone, *sensu Melchin et al.*, 2013], the land-ice front temporarily retreats over Gondwana [*Sutcliffe et al.*, 2000; *Loi et al.*, 2010; *Moreau*, 2011] and tropical SSTs increase back [*Finnegan et al.*, 2011; *Melchin et al.*, 2013], which lead some authors to consider this event as an interglacial [*Denis et al.*, 2007; *Ghienne et al.*, 2007; *Loi et al.*, 2010; *Young et al.*, 2010; *Moreau*, 2011; *Melchin et al.*, 2013]. *Pohl et al.* [2014] proposed that the non-linear Ordovician temperature response, simulated in this study when decreasing solar luminosity from 345 $W.m^{-2}$ to 344 $W.m^{-2}$, may provide an explanation to the otherwise enigmatic sudden Hirnantian climate cooling. This hypothesis suggests that the simulation conducted at 344 $W.m^{-2}$ may be the most representative of the Hirnantian climate. Although this very cold state may adequately represent the periods of Hirnantian glacial advance, we here focus on the mid-Hirnantian interglacial when climate was significantly warmer as testified by the retreat of the ice front in North Africa and in the Middle East [e.g., *Ghienne et al.*, 2007; *Moreau*, 2011]. We therefore consider that the simulation at 345 $W.m^{-2}$ best reflects the climatic conditions prevailing during the mid-Hirnantian interglacial (Fig. 2A). The annual-mean, globally-averaged surface air temperature in this model run is 17.1 °C, compared to 23.4 °C at 350 $W.m^{-2}$. From a radiative point of view, a halving of the atmospheric $CO_2$ concentration corresponds to a radiative perturbation of –3.7 $W.m^{-2}$ at the top of the atmosphere [*Myhre et al.*, 1998]. The decrease in solar luminosity accounting for the Hirnantian climate cooling in our simulations (from 350 $W.m^{-2}$ to 345 $W.m^{-2}$) is therefore equivalent to a decrease of $pCO_2$ by a factor 2.7, or equally to a decline of $pCO_2$ from 8 PAL (or 12 PAL) during the late Katian to 3 PAL (4.5 PAL). The magnitude of this decrease in radiative forcing is in reasonable agreement with the estimates recently proposed by *Pohl et al.* [2016b]. Using an innovative coupling method between climate models and an ice-sheet model, they conducted the first simulation of Ordovician land-ice growth that is supported by the geological record. In their models, best match with data is obtained between 8 PAL and 12 PAL during the late Katian, and at 3 PAL during the Hirnantian (see their Fig. 9). We emphasize that we do not investigate the climatic impact of the growth of the Hirnantian ice sheet over the South Pole in the present study but identify this as a target for the future.

The latest Hirnantian-early Rhuddanian period is characterized by the continental-scale decay of the Gondwana ice sheet [*Finnegan et al.*, 2011; *Moreau*, 2011; *Denis et al.*, 2007; *Loi et al.*, 2010; *Le Heron et al.*, 2009]. *Trotter et al.*'s (2008) data do not extend into the Silurian, thus hampering any appraisal of the climatic conditions relative to Mid-Ordovician levels. The clumped-isotope analysis of *Finnegan et al.* [2011], however, suggests that tropical SSTs rapidly rise in the aftermath of the Hirnantian glacial peak and reach pre-Hirnantian levels as early as the latest Hirnantian (~ 35 °C). This value is supported by the Telychian (~ 435 Ma) estimate of 34.9 ± 0.4 °C reported by *Came et al.* [2007] in a previous study on Anticosti Island. We therefore assume that the solar forcing level chosen previously to study the Katian (350 W.m$^{-2}$) satisfactorily represents the Rhuddanian time slice as well (Fig. 2A).

## 4 The late Katian

In the compilation of *Melchin et al.* [2013], black shale deposition in the late Katian occurred mainly at tropical to subtropical paleolatitudes on the western margin of the equatorial landmasses. On the contrary, the northern margin of Gondwana and the platforms surrounding Baltica were typified by oxic deposits (see Fig. 3A). Here we examine the simulation conducted at 350 W.m$^{-2}$ in order to disentangle the respective contributions of surface primary productivity and dissolved oxygen concentration in the formation of the pre-Hirnantian black shales.

### 4.1 Simulating the late Katian marine primary productivity

Figure 3A displays the NPP simulated using a solar forcing level of 350 W.m$^{-2}$, together with the individual contributions of phosphate concentration (Fig. 3B, $3^{rd}$ term in Eq. 1) and photosynthetically active radiation (Fig. 3C, $2^{nd}$ term in Eq. 1) in the simulated NPP. While the limitation in $PO_4$ (Fig. 3B) is the main driver of the primary productivity pattern (Fig. 3A), the availability of light imposes a hemispheric-scale decrease of the productivity with latitude (Fig. 3C).

The distribution of $PO_4$ (Fig. 3B) in the surface waters is controlled by the large-scale pattern of vertical velocities just below the surface of the ocean, which are dominated by Ekman pumping/suction [Ekman transport, *Ekman*, 1905]. *(i)* Along the equator, the Trade Winds induce the divergence of the ocean water masses, resulting in equatorial upwelling (Fig. 3D, see also Fig. 4). These equatorial winds further drive offshore Ekman transport

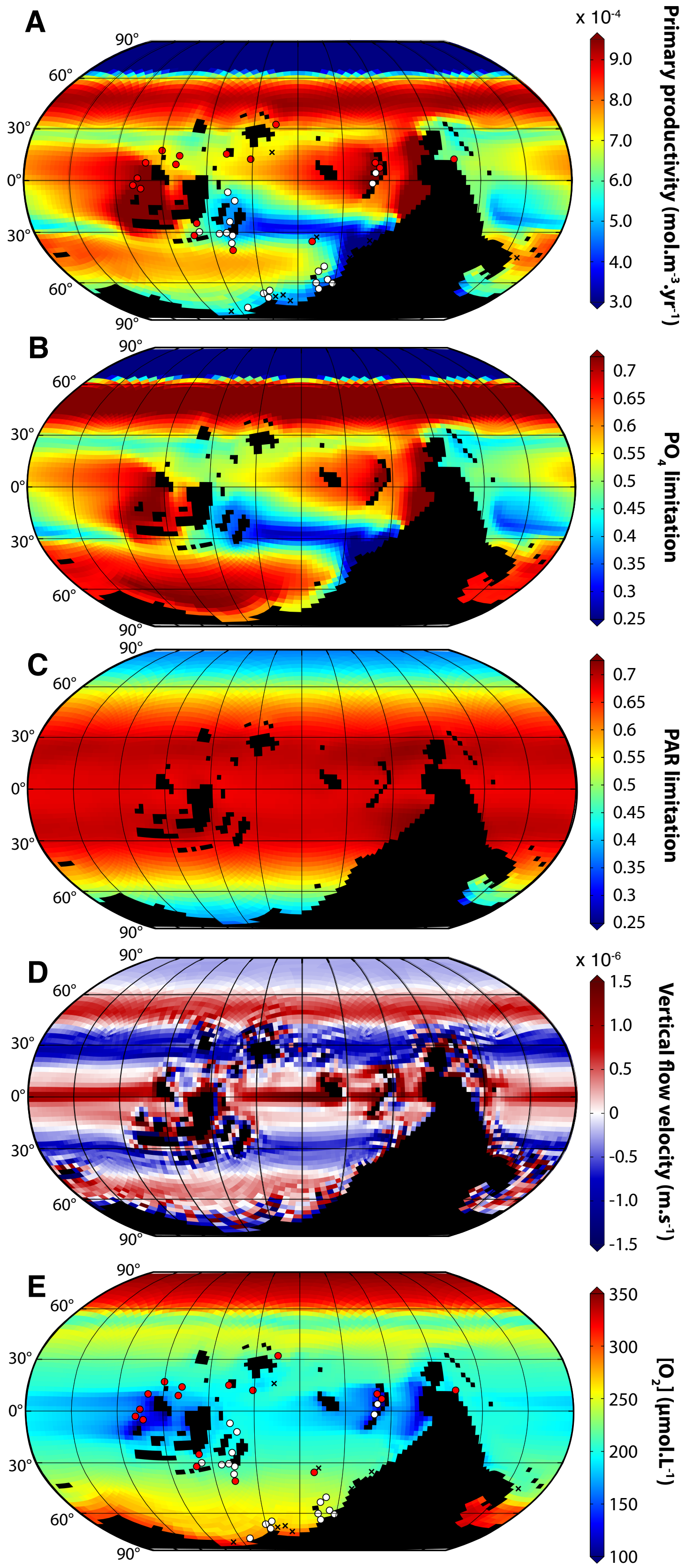


**Figure 3.** Analysis of the patterns of marine primary productivity and oxygen concentration simulated using the 440 Ma land-sea mask and a solar forcing level of 350 W.m$^{-2}$. (**A**): Surface primary productivity. White and red dots respectively stand for sediments of Katian age associated with dysoxic-to-oxic and at least intermittently anoxic conditions (i.e.,black shales, including interbedded black shales), after the compilation of *Melchin et al.* [2013]. (**B**): Contribution of surface phosphate concentration to the primary productivity (3$^{rd}$ term in Eq. 1). (**C**): Contribution of the PAR to the surface primary productivity (2$^{nd}$ term in Eq. 1). (**D**): Vertical velocity averaged over the first 50 m of the water column. Positive values correspond to up-

along the western margin of the tropical continental masses, i.e., Laurentia, South China-Annamia and the Gondwana, allowing cold, nutrient-rich water to upwell from the deep ocean (Fig. 3D ; see Fig. 1 for the name and location of each continent). An intense surface primary productivity is therefore simulated at these latitudes (Fig. 3A). *(ii)* Low levels of phosphate concentration are simulated around 30° S and 30° N (Fig. 3B). Between the Trades, at tropical latitudes, and the Westerlies, at the mid-latitudes, the ocean realm centered on 30° N/S is typified by the convergence and sinking of low-phosphate surface waters (Fig. 3D). This corresponds to the poleward edge of the tropical cells of the oceanic overturning circulation (Fig. 4D). In the Paleo-Tethys, between eastern Baltica and the western coast of Gondwana (Fig. 5A), the downwelling of surface waters further combines with a strong freshwater flux from the continent (Fig. 5B,C), forming a zone of minimum phosphate concentration (Fig. 5A) and thus minimum primary productivity (Fig. 3A). In detail, moisture-laden air masses originating from the Paleo-Tethys are conveyed by the Westerlies to the western coast of Gondwana. Further inland, intense orographic precipitation occurs and the amount of liquid water exceeding the field capacity of the soil is delivered to the ocean (Fig. 5C), where the freshwater flux induces a strong dilution of both salinity (Fig. 5B) and phosphate (Fig. 5A). It is noteworthy that, using the same paleogeography but another ocean-atmosphere general circulation model employing an explicit routing scheme for runoff and a more sophisticated atmospheric component [FOAM, *Jacob*, 1997], *Pohl et al.* [2016a] simulated very similar regional patterns of runoff and freshwater input to the ocean (Fig. S3). In addition, most Ordovician paleogeographical reconstructions seem to concur regarding the presence of highlands over Gondwana at these latitudes, that are likely to promote intense precipitation and runoff along the western coast of the supercontinent [*Blakey*, 2016; *Scotese*, 2016]. *(iii)* Between 40° and 60°, the Westerlies drive an equatorward Ekman transport and deep-water upwelling (Fig. 3D). The dynamical regime of the Northern high-latitudes Ordovician is similar to that seen in the present-day Southern Ocean with its Antarctic Circumpolar Current [*Marshall and Speer*, 2012, see Fig. 4]. As a consequence phosphate-rich waters are brought up to the ocean surface (Fig. 3B) where they fuel the surface primary productivity (Fig. 3A). *(iv)* Whereas the Northern Hemisphere polar latitudes (60°–90°) are dynamically isolated from the global ocean (Fig. 4B) and thus depleted in nutrients (Fig. 3B), the Southern high-latitudes are typified by a strong nutrient supply (Fig. 3B). The latter spatially correlates with a deep mixed layer (Fig. 5D,E) and results from the intense deep convection and intense vertical exchange with nutrient-rich deep waters along the northern margin of Gondwana (Fig. 4B). The location of this zone of intense convection is supported by previous studies [e.g., *Herrmann et al.*, 2004, see also Fig S4]. In the Southern Hemisphere, combined imprints of the Westerlies (at the mid-latitudes) and of deep-water convection (at polar latitudes) result in a large zone of nutrient-rich waters extending from ~ 40° S to the South Pole (Fig. 3B). Over the Pole along the coast of Gondwana, however, the high levels of phosphate concentration do not directly translate into intense primary productivity (Fig. 3A) because of the limited incoming solar radiation (Fig. 3C).

### 4.2 Black shale deposits and the redox state of the ocean

Comparison of the patterns of simulated primary productivity with the database of *Melchin et al.* [2013] (Fig. 3A) reveals an interesting match between high-productivity areas (low-productivity areas) and geologically-testified preservation of black shales (oxic deposits). This correlation is summarized with boxplots in Fig. 6A.

We seek to determine whether the difference between the primary productivity simulated at localities typified by the deposition of black shales on the one hand, and typified by oxic conditions on the other hand (after *Melchin et al.*, 2013; see Fig. 3A and Fig. 6A), is significant from a statistical point of view. We choose the Wilcoxon-Mann-Whitney test [*R Core Team*, 2013]. This is a basic nonparametric test of the null hypothesis that the two samples come from the same population (H0: levels of primary productivity simulated where black shales are preserved do not significantly differ from the values simulated where oxic deposits are documented). The alternative hypothesis is that a particular population tends to have larger values than the other (H1: primary productivity in the model is significantly higher where black shales are preserved than they are at oxic localities). Unlike the *t*-test, the Wilcoxon-Mann-Whitney test does not require the assumption of normal distributions, which is crucial in our study given the limited number of Ordovician observations in *Melchin et al.*'s (2013) database. The result of the test is expressed as a *p*-value. If the *p*-value is less than the significance level chosen (e.g., $p$-value $< 0.05$), then the test suggests that the observed data is inconsistent with the null hypothesis, so the null hypothesis H0 must be rejected and the alternative hypothesis H1 accepted: the two samples do not come from the same population.

The Wilcoxon-Mann-Whitney test confirms that the two samples – the black shales and oxic deposits, red and white data points in Fig. 3A – represent two populations charac-

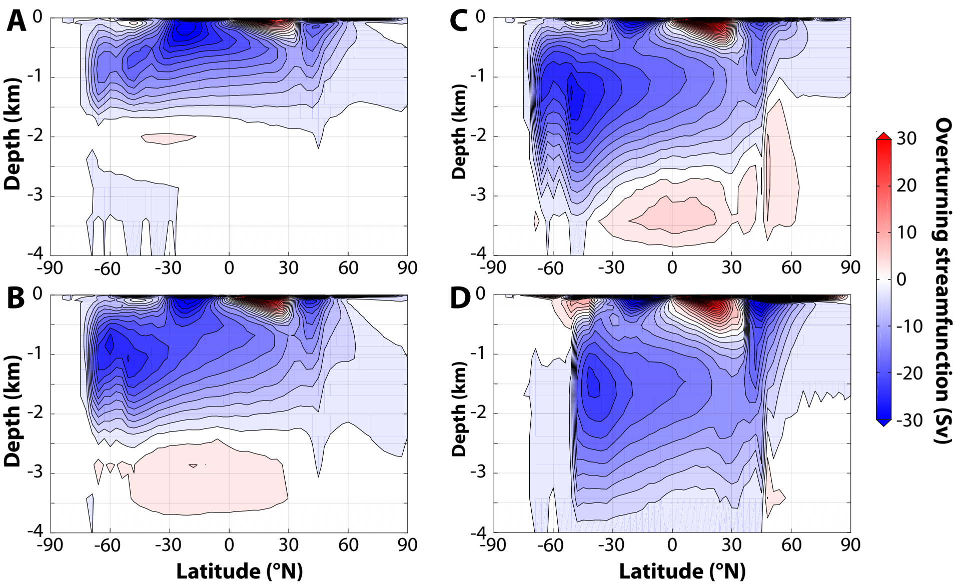


**Figure 4.** Meridional overturning streamfunction simulated using solar constant values of (**A**): 355 W.m$^{-2}$; (**B**): 350 W.m$^{-2}$; (**C**): 345 W.m$^{-2}$ and (**D**): 344 W.m$^{-2}$. The streamfunction is computed as the sum of the Eulerian and eddy-induced circulations. The contour interval is 2.5 Sv (Sverdrup, 1 Sv = 10$^{6}$ m$^{3}$.s$^{-1}$). A negative (blue) streamfunction corresponds to an anticlockwise circulation. Results from the two end-member model runs conducted at 355 W.m$^{-2}$ and 344 W.m$^{-2}$ are shown here to highlight the deepening trend in the meridional overturning streamfunction. They are not discussed in the main text. Main patterns of the simulated overturning streamfunction are in agreement with previous studies of *Poussart et al.* [1999] and *Herrmann et al.* [2004].

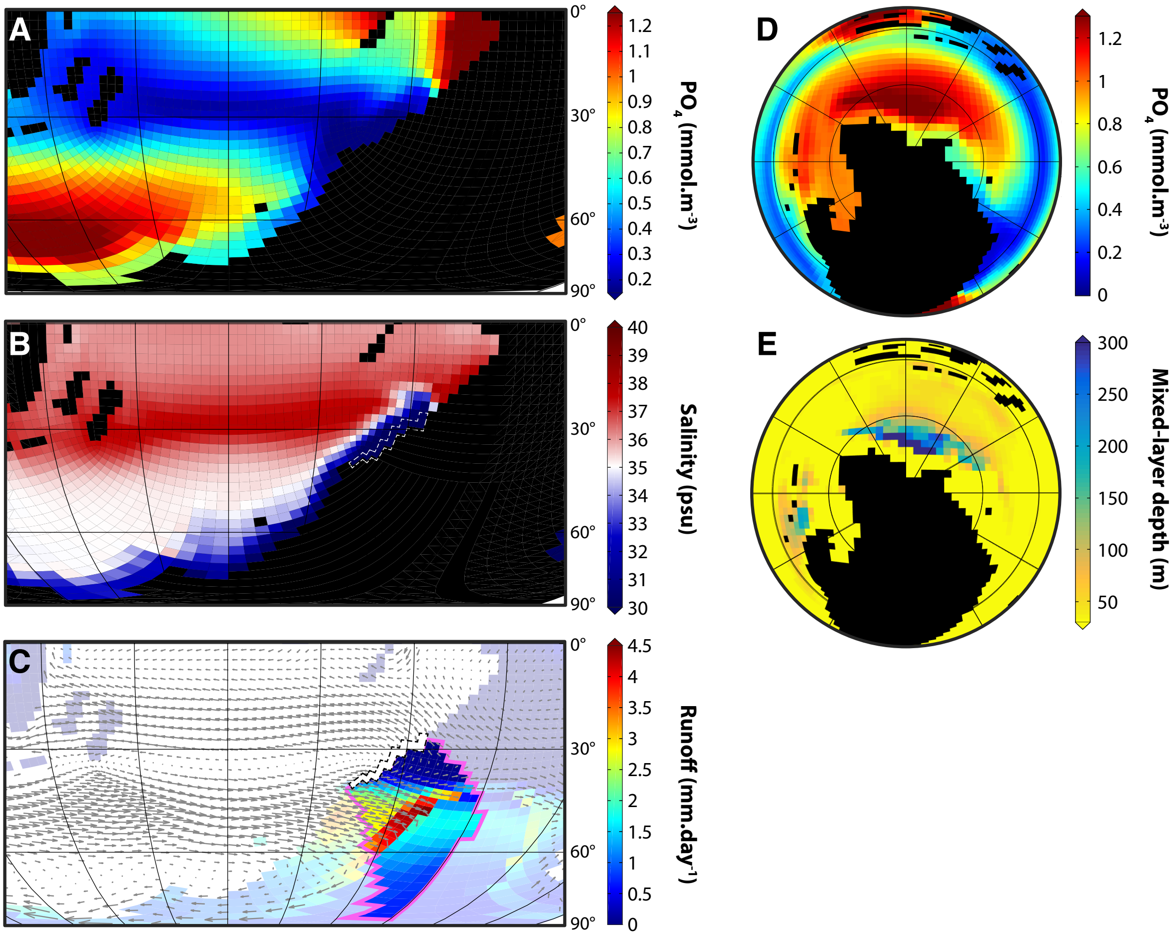


**Figure 5.** Analysis of the patterns of mean annual, surface phosphate concentration simulated using the 440 Ma continental land-sea mask and a solar forcing level of 350 W.m$^{-2}$. **(A)**: $PO_4$ concentration in the Paleo-Tethys. **(B)**: Ocean surface salinity in the Paleo-Tethys. **(C)**: Near-surface winds (vectors) and continental runoff (shading) simulated in the same region. The pink contour delimits the watershed associated with the outlet constituted by the points highlighted with the dashed white line in subplot **B**, which correspond in turn to a zone of minimum of salinity. Grid points with no vectors are mountainous areas. Runoff here refers to the amount of water that is transferred from the continental grid points to the ocean (no routine scheme is implemented in this configuration of the model, see Sect. 2.1.1). **(D)**: South-polar projection map of surface phosphate concentration. Laurentia is shown on top of the map. **(E)**: South-polar projection map of mixed-layer depth.

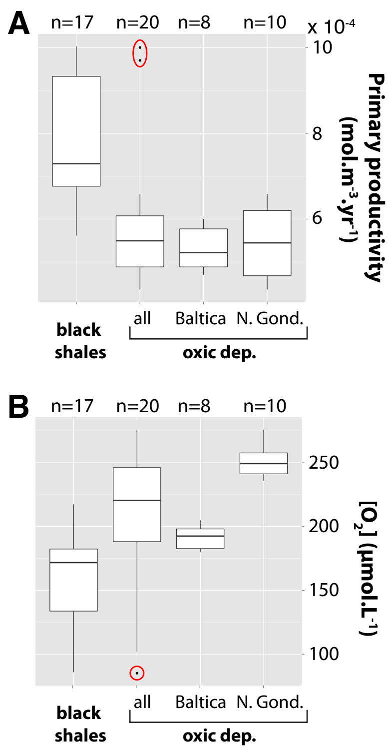


**Figure 6.** Boxplots of primary productivity at the ocean surface **(A)**, and oxygen concentration at the depth of the epicontinental seas (80 m) **(B)**, simulated using the 440 Ma land-sea mask and a solar forcing level of 350 $W.m^{-2}$ at each Katian data point from *Melchin et al.* [2013]. For statistical analysis, points are gathered into samples depending on whether sediments were deposited under oxic ("oxic dep., all") or anoxic conditions ("black shales"), after *Melchin et al.*, 2013 (white and red dots in Fig 3A, respectively). Oxic sediments situated around Baltica (see "Baltica" in the legend) and along the margin of Gondwana ("N. Gond.") are further extracted for dedicated investigation. The group gathering all the *n=20* "oxic deposits" points therefore includes the *n=8* data points around Baltica, plus the *n=10* data points situated along the northern margin of Gondwana and the two points between South China and Annamia (i.e., the two outliers in subplot **A**, see Fig. 3A). The box represents the inter-quartile range (or $IQR$, i.e., distance between the first and the third quartiles) and the band inside the box is the second quartile (i.e., the median). The upper and lower whiskers respectively extend from the box to the highest (lowest) value that is within $1.5 * IQR$ beyond the box edges, and data beyond the end of the whiskers (circled in red) are outliers, following *Tukey* [1977].

terized by significantly distinct levels of primary productivity ($p$-value: 6.53 x $10^{-5}$ < 0.05, H0 is rejected). Three different sets of points can be distinguished within the oxic data points reported by *Melchin et al.* [2013]. The first group is composed of the two outliers deduced from Fig. 6A. They correspond to the two points located in the high-productivity area along the western coast of South China and Annamia (Fig. 3A). Other data points can be gathered into two groups depending on whether they belong to the cluster of points situated around Baltica or along the northern margin of Gondwana (Fig. 3A). Interestingly, both clusters seem to be relatively similar to each other (Fig. 6A), and a Wilcoxon-Mann-Whitney test confirms that they come from the same statistical population ($p$-value: 0.762 > 0.05, H0 is accepted). It appears that the correlation between low marine productivity and oxic deposition is relatively strong, except for the two outliers highlighted previously.

At the depth of the epicontinental shelves, the oxygen concentration increases from the equator to the poles (Fig. 3E). This gradient reflects the higher solubility of oxygen in cold waters. Superimposed on this purely thermal effect is the imprint of ocean dynamics. The western margin of the equatorial continental masses, in particular, is washed by oxygen-poor waters upwelling from deeper parts of the ocean. Because they are rich in nutrients, these waters promote regional primary productivity (Fig. 3A), which in turn increases remineralization in the water column and thus enhances oxygen depletion at depth. Geological evidence for organic matter preservation spatially correlates with oxygen levels that are, in the model, significantly lower than those simulated at oxic localities (Figs. 3E and 6B, $p$-value: 0.0016 < 0.05 for the two-sided Wilcoxon-Mann-Whitney test). However, the points associated with conditions of oxic sedimentation actually include two significantly contrasting populations ($p$-value: 4.571 x $10^{-5}$ < 0.05): the points clustering along the coast of Gondwana are typified by high oxygen levels, whereas the points around Baltica do not significantly differ from the “black shale” population (Fig. 6B, $p$-value: 0.075 > 0.05).

### 4.3 Sensitivity to the $pO_2$

The regions where black shales are preserved in the Katian sedimentary record [*Melchin et al.*, 2013] correlate well with the areas of high surface primary productivity simulated under a warm climate representative of pre-Hirnantian conditions. Conversely, the preservation of sediments testifying of oxic depositional settings is documented in regions where the simulated primary productivity is low. The spatial correlation between geological proxies of ocean redox state and simulated oxygen concentration is less obvious. These results suggest that the spatial distribution of the black shales deposited during the Katian may have been mainly driven, at a global scale, by surface primary productivity levels rather than variations in dissolved oxygen concentration.

Nevertheless, when it is run on the present-day continental configuration, our model simulates, over extended areas that are devoid of black shales today, levels of surface primary productivity that reach the values associated with the deposition of black shales during the Katian (Fig. S5). This points to major differences between the Ordovician and present-day oceans, that would have augmented the potential for organic matter burial in the Early Paleozoic.

Biogeochemical models and inversion methods notably indicate that the $pO_2$ was significantly lower in the Ordovician, probably between 0.2 and 0.8 times the present-day levels [*Bergman et al.*, 2004; *Berner*, 2006; *Algeo and Ingall*, 2007; *Berner*, 2009; *Lenton et al.*, 2016]. Sensitivity tests confirm that atmospheric oxygen levels in this range significantly reduce the oxygenation of the ocean at the depth of the epicontinental seas in the model (Fig. 7; see also Fig. S6 for depth profiles over the whole water column). Between 0.4 and 0.2 PAL $O_2$, the tropics exhibit low concentrations of dissolved oxygen (< 75 $\mu$mol.L$^{-1}$) that would significantly reduce the rate of degradation of the settled organic matter (Fig. 7D-E). The absence of charcoal in the Ordovician sedimentary record further suggests that the $pO_2$ was sufficiently low as to prevent the sustained combustion of plant material [< 13 %, *Chaloner*, 1989; *Algeo and Ingall*, 2007], supporting the lowest estimates from the $pO_2$ range above. With a $pO_2$ set to 0.2 times the present-day level, the ocean oxygen content drops below 50 $\mu$mol.L$^{-1}$ over virtually the entire ocean realm, except in the Northern Hemisphere highest latitudes and at the location of deep-water formation in the Southern Hemisphere (Fig. 7E).

We argue that the lowered Early Paleozoic $pO_2$ ($\leq$ 0.4 PAL $O_2$, Fig. 7), combined with exceptionally vast shallow-water environments [*Walker et al.*, 2002] resulting from the highest sea level during the whole Paleozoic Era [*Haq and Schutter*, 2008], largely predisposed the Ordovician ocean to organic matter preservation. Our results suggest that, in this particular context, the deposition of black shales in tropical settings may have been driven by the patterns of surface primary productivity. Our simulations also imply that the two data points characterized by unexpected oxic depositional settings in South China – the two outliers highlighted in Fig. 6A, points No. 25 and No. 26 from *Melchin et al.* [2013] – may re-

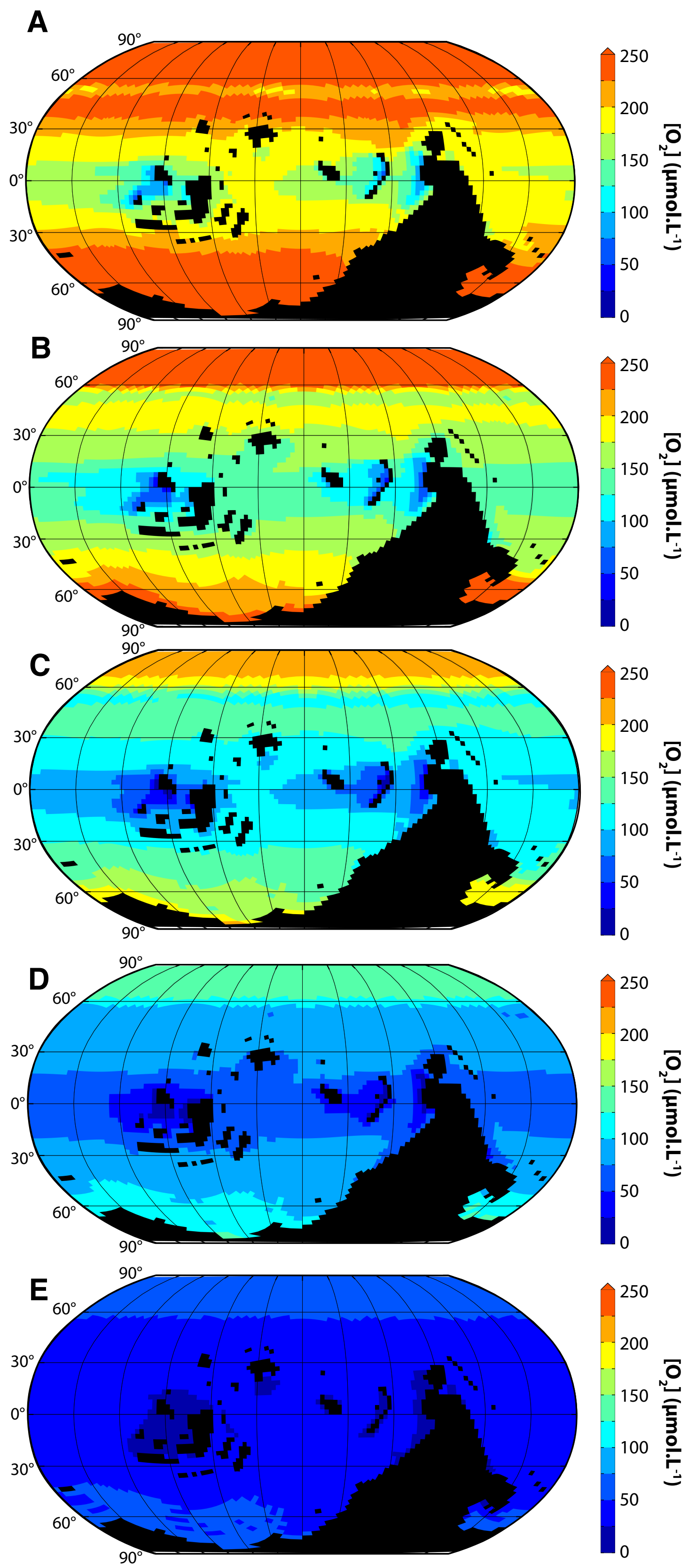


**Figure 7.** Sensitivity test to the $pO_2$: oxygen concentration simulated at the depth of the epicontinental seas in the model (80 m), using the 440 Ma land-sea mask, a solar forcing level of 350 W.m$^{-2}$ and an atmospheric $pO_2$ set to **(A)**: 1.0, **(B)**: 0.8, **(C)**: 0.6, **(D)**: 0.4, and **(E)**: 0.2 times the present-day value.

flect local redox conditions typifying basins that were at least partially disconnected from the open ocean.

## 5 The Hirnantian glacial pulse

The latest Ordovician Hirnantian is characterized by a sudden drop in tropical SSTs [*Trotter et al.*, 2008; *Finnegan et al.*, 2011]. It represents the climax of the Ordovician glaciation [*Page et al.*, 2007; *Finnegan et al.*, 2011; *Pohl et al.*, 2016b]. The compilation of *Melchin et al.* [2013] reports a worldwide change to more oxygenated depositional settings at this time. In order to investigate the mechanisms driving this possible mid-Hirnantian oceanic oxygenation event, we here study the response of Ordovician marine biogeochemistry to climate cooling.

### 5.1 Response of the ocean redox state to climate cooling

For these experiments, we lower the incoming solar radiation in order to simulate a climate cooling (from 350 W.m$^{-2}$ to 345 W.m$^{-2}$, see Sect. 3). As a consequence tropical SSTs drop from 32.5 to 29.2 °C (Fig. 2A). This also artificially induces a slight (ca. –1.5 %) decrease in simulated net primary productivity, through a drop in photosynthetically available radiation, following Eq. 1.

Climate cooling does not critically impact the first-order patterns of simulated primary productivity (Fig. 8A). The prominent change accompanying the drop in temperature is the increase in oxygen concentration throughout the water column (Fig. 8B). The latter results from two main mechanisms. First, oxygen solubility in ocean water increases with decreasing temperature. A straightforward effect of this is a more intense air-sea exchange of oxygen at the ocean surface in the coldest simulation. This directly affects the first tens of meters of the water column, the so-called mixed layer, and then the deeper layers as currents and mixing processes carry the enhanced surface oxygenation in the ocean interior (Fig. 8B). Second, the meridional overturning circulation intensifies and deepens (compare Figs. 4B and 4C) in response to climate cooling and associated sea-ice spread (Fig. 2B), thus enhancing the ventilation and the oxygenation of the deep ocean. Interestingly, the oxygenation of the deep ocean is not uniform in space. As shown in Figs. 8C and D, the increase in ocean bottom oxygen concentration reaches its maximum where Ordovician deep waters form (see Fig. 5E). On the contrary, the water masses that sink along the northern margin of Gondwana do not enter the Paleo-Tethys realm, which is virtually isolated from the global ocean. This area is characterized by low oxygen levels in the 350 $W.m^{-2}$ model run, with a global minimum located over South China-Annamia (Fig. 8C). When solar forcing is decreased, the whole Paleo-Tethys displays a very limited $pO_2$ increase (Fig. 8D). Results of additional simulations using a $pO_2$ reduced to 0.4 times the present-day value (see Sect. 4.3) confirm that it is difficult to reach deep-ocean anoxia during the Hirnantian (Fig. S7). While most of the ocean bottom is suboxic to anoxic under Katian climatic conditions (i.e., dissolved oxygen levels below 25 $\mu mol.L^{-1}$), deep-ocean oxygen values stay above 25 $\mu mol.L^{-1}$ everywhere, except in the Paleo-Tethys, under Hirnantian conditions (i.e., solar forcing dropped to 345 $W.m^{-2}$).

Our simulations do not account for the drop in continental weathering that should accompany climate cooling [*Le Hir et al.*, 2009; *Beaulieu et al.*, 2012]. The latter would be at least one order of magnitude higher than the $\sim$ 1.5 % decrease in PAR associated with the lower solar luminosity used to simulate Hirnantian climate, thus further reducing modeled net primary productivity and strengthening the oxygenation of the water column through decreased remineralization.

### 5.2 Discussion: the Hirnantian oxygenation event

The sediments preserved in relatively shallow environments record a worldwide shift from less oxygenated to more ventilated depositional settings during the Hirnantian [*Melchin et al.*, 2013], which is consistent with the general oxygenation trend accompanying climate cooling in our runs. The redox state of the ocean interior, however, remains the subject of hot controversy. Depending on the proxies, the Hirnantian ocean is described as undergoing vigorous sea floor oxygenation [*Armstrong and Coe*, 1997; *Page et al.*, 2007; *LaPorte et al.*, 2009; *Zhou et al.*, 2012; *Melchin et al.*, 2013], or deep-water anoxia [*Brenchley et al.*, 1994; *Hammarlund et al.*, 2012; *Zhang et al.*, 2009]. Such uncertainties are, at least partly, rooted in the intrinsically lacunar nature of the Early Palaeozoic sedimentary record. Due to the lack of preservation of pre-Mesozoic ocean bottom sediments [*Cramer and Saltzman*, 2007a], deep-ocean redox conditions must be reconstructed based on ocean proxies preserved in shelf or slope settings [*Hammarlund et al.*, 2012; *Melchin et al.*, 2013]. The possibility of an Hirnantian deep-water oxygenation event [*Zhou et al.*, 2012] is supported by geochemical data. *LaPorte et al.* [2009] and *Melchin et al.* [2013] notably report a positive $\delta^{15}N$ excursion, that they interpret as a decreased contribution of cyanobacterial N fixation to the phytoplankton productivity, representative of a more oxygenated ocean during the glacial pulse. Based on

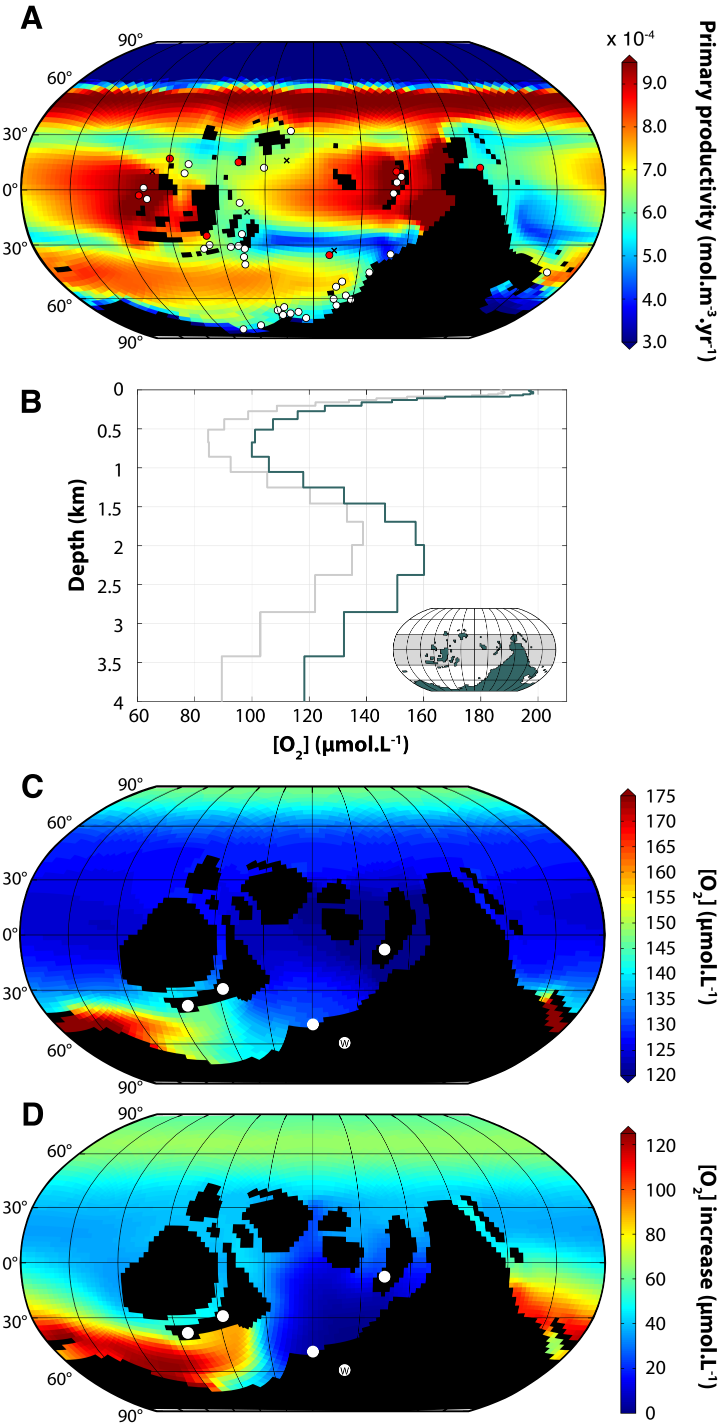


**Figure 8.** Impact of climate cooling on the primary productivity simulated at the ocean surface and on the oxygen concentration simulated throughout the water column. (**A**): Marine primary productivity simulated using the 440 Ma land-sea mask and a solar forcing level of 345 W.m$^{-2}$. White and red dots respectively stand for sediments of Hirnantian age associated with dysoxic-to-oxic and intermittently anoxic conditions (i.e., interbedded black shales), after the compilation of *Melchin et al.* [2013]. No continuous black shale deposition is reported during the Hirnantian. See Fig. S2 for data points labeling. (**B**): Depth profiles of mean annual, tropical oxygen concentration simulated using the 440 Ma land-sea mask and solar forcing values of 350 W.m$^{-2}$ (light grey curve) and 345 W.m$^{-2}$ (dark grey curve). The insert in the bottom-right corner represents the area over which data were averaged. The plot focuses on the tropical ocean, where major shifts in redox conditions are documented from the Katian to the Hirnantian [*Melchin et al.*, 2013]. (**C**): Oxygen concentration simulated at the ocean bottom at 350 W.m$^{-2}$. (**D**): Increase in ocean bottom oxygen

the analysis of various redox proxies of the ocean, *Zhou et al.* [2012] further suggest that the Ordovician-Silurian transition is characterized by persistent basinal anoxia, with the exception of an intense oxygenation event during the Hirnantian. On the contrary, *Zhang et al.* [2009] and *Hammarlund et al.* [2012], although they agree on the oxic nature of the shallow-water deposits during the Hirnantian, document a positive excursion in the stable isotope compositions of sedimentary pyrite sulfur ($\delta^{34}S_{pyr}$; see also *Yan et al.*, 2009), that they explain by enhanced burial rates of pyrite in the context of deep-water anoxia during the same period of time. Interestingly, *Jones and Fike* [2013] recently rejected this theory based on new paired sulfate-pyrite $\delta^{34}S$ data from Anticosti Island. In their geochemical record, they observe the positive enrichment in $\delta^{34}S_{pyr}$ previously reported by *Hammarlund et al.* [2012] and *Zhang et al.* [2009], but no parallel excursion in carbonate-associated sulfate ($\delta^{34}S_{CAS}$). Based on geochemical modeling, they demonstrate that an increase in pyrite burial strong enough to generate a sulfur isotope excursion during the Hirnantian would necessarily induce a parallel excursion of equal magnitude in the isotopic composition of coeval marine sulfate. The absence of such parallel excursion in their $\delta^{34}S_{CAS}$ record therefore preclude enhanced pyrite burial as the cause of the Hirnantian $\delta^{34}S_{pyr}$ excursion. Results from our general circulation model suggest that the climate cooling associated with the Hirnantian glacial pulse induces an increase in oxygen concentration throughout the water column. They support the visions of a better-ventilated Hirnantian deep ocean [*Melchin et al.*, 2013; *LaPorte et al.*, 2009; *Zhou et al.*, 2012; *Jones and Fike*, 2013].

The hypothesis of a well-oxygenated Hirnantian ocean brings crucial insights into the mechanisms that possibly drove the turnovers in marine living communities reported for that time period. The Late Ordovician extinction is one of the "big five" mass extinctions that punctuated the Phanerozoic [*Servais et al.*, 2010], with the disappearance of about 85 % of all marine species [*Sheehan*, 2001; *Harper et al.*, 2013a]. The coincidence of the two pulses of the extinction event with respectively the onset and demise of the Hirnantian glacial maximum, suggests that these abrupt environmental changes caused the extinction [e.g. *Sheehan*, 2001]. The precise underlying mechanisms, however, are still a matter of debate [*Luo et al.*, 2016]. While the global spread of anoxia, in the context of the post-glacial transgression, is generally admitted to explain the second pulse of the extinction [*Harper et al.*, 2013a; *Melchin et al.*, 2013; *Luo et al.*, 2016], a general consensus about the kill mechanisms implied in the first phase of the event is still lacking [*Harper et al.*, 2013a]. It is often considered that the global climate cooling and eustatic sea-level fall lead to a critical habitat destruction [*Sheehan*, 2001]. The intensification in ocean ventilation may also have strongly stricken the fauna adapted to the pre-glacial sluggish ocean circulation and associated ocean-water chemistry [*Berry et al.*, 1990]. Contrasting to this, however, *Hammarlund et al.* [2012] and *Zhang et al.* [2009] recently proposed the development of deep-water anoxia as a primary kill mechanism during the first event of the faunal mass extinction. Based on the temporal correlation between the enrichment of ocean water in harmful metals (potentially under oxygen-depleted conditions) on the one hand, and high rates of plankton malformations and extinction of marine species on the other hand, *Vandenbroucke et al.* [2015] further supported the role of anoxia as a dominant kill mechanism through the Ordovician-Silurian transition. Our findings suggest that the ocean was generally better ventilated during the Hirnantian glacial event than it was before it, and do not support an Hirnantian oceanic anoxic event as the primary cause for the first pulse of the Late Ordovician extinction.

We also note that some of the data on which the latter hypothesis is based come from the margins of the Paleo-Tethys. This is notably the case for the samples of *Zhang et al.* [2009], from South China, and for the Carnic Alps section of *Hammarlund et al.* [2012], which was located along the northern margin of Gondwana during the Ordovician (Fig. 8C-D). Similarly, the metal content measurements of *Vandenbroucke et al.* [2015] were conducted on samples obtained from a well situated in the Libyan desert, on the northern margin of Gondwana, in a region that was washed by the waters from the Paleo-Tethys as well (Fig. 8C-D). We showed that the Paleo-Tethys is characterized by a low sea-floor oxygenation under a warm climate. We further demonstrated that, when a cooling is applied, this region remains dynamically insulated from the global ocean. Here, the increase in ocean bottom oxygen concentration is minimum. This particular Paleo-Tethysian context therefore suggests that some of the data that served to the construction of the paradigm of an Hirnantian oceanic anoxic event may be of regional significance. This hypothesis is supported by several geochemical studies demonstrating that at least some of the trace metal accumulations measured by *Vandenbroucke et al.* [2015] (Fe, Mo, Pb, Mn, Ba, As) are recorders of local rather than global redox conditions [e.g., *Hoffman et al.*, 1998; *Algeo and Maynard*, 2008; *Och et al.*, 2015; *Owens et al.*, 2017].

## 6 The early Silurian Rhuddanian oceanic anoxic event

Following the mid-Hirnantian oxygenation event, the early Silurian represents the worldwide spread of anoxia [*Melchin et al.*, 2013]. While a return to a warmer climate, in the context of the Hirnantian deglaciation, may provide a valid explanation to the deposition of black shales at tropical latitudes, we have shown previously that it would not explain the preservation of organic-matter-rich deposits around Baltica and over the South Pole, along the coast of Gondwana (Sect. 4.2). This requires additional mechanisms. So far, two main theories have been proposed: *(i)* stratification of the water column and oxygen depletion at depth, through the input of freshwater during the melt of the Gondwana ice-sheet [*Armstrong et al.*, 2005, 2009; *Melchin et al.*, 2013], and *(ii)* increased primary productivity fueled by the release of nutrients during the weathering of newly-exposed glaciogenic sediments experiencing climate warming [*Armstrong et al.*, 2005, 2009; *Le Heron et al.*, 2013]. Below, we use our general circulation model of the ocean to test each of these hypotheses.

### 6.1 Impact of a freshwater flux

The freshwater flux associated with the melt of the Gondwana ice sheet may have significantly slowed down the formation of deep water over the South Pole, promoting water column stratification, oxygen impoverishment and thus organic matter preservation at depth. This scenario has been proposed to explain the deposition of black shales during the early Silurian [*Armstrong et al.*, 2005, 2009; *Melchin et al.*, 2013]. It is also supported by recent studies highlighting the critical role of ocean dynamics in the ventilation of the deep ocean and thus in the likelihood that the Earth System may be affected by an oceanic anoxic event [*Donnadieu et al.*, 2016]. In models, increased freshwater fluxes to the ocean (e.g. from ice-sheet melting) often result in a significant weakening of the overturning circulation. This effect can be associated with an hysteresis behavior, whereby the overturning does not fully recover once the freshwater perturbation stops [*Stommel*, 1961; *Rahmstorf*, 1996, and many others]. The impact of a freshwater flux on the Ordovician ocean circulation has never been quantified, and such hypotheses remain essentially speculative so far.

Here, we build on numerous previous studies [see for example *Kageyama et al.*, 2013, and references therein] to conduct, for the first time, freshwater hosing experiments in the Silurian. We restart our model from the mid-Hirnantian climatic steady-state (345 $W.m^{-2}$, see Sect. 5) and we run a transient simulation, by *(i)* imposing a freshwater perturbation for 500 years, and *(ii)* integrating the model for 500 additional years once the freshwater perturbation stops. This allows us to investigate both the response of the ocean circulation to a melt-water pulse, the duration of which is of the same order as the abrupt events of the last glacial [*Roche et al.*, 2004], and its potential recovery, once the perturbation has come to an end. While regions of melt water discharge have been the subject of comprehensive investigation for the last deglaciation [*Roche et al.*, 2009], virtually no constraints are available in the Ordovician. Freshwater can reach the open ocean at various locations, ranging from the outlet of the rivers draining the glacial watersheds to icebergs melt zones [*Roche et al.*, 2009]. Given the large uncertainties in reconstructing both the topography of Gondwana [*Blakey*, 2016; *Scotese*, 2016] and its land-ice cover [*Le Heron and Dowdeswell*, 2009], defining zones of preferential meltwater release seems elusive. In order to simultaneously account for icebergs and coastal runoff from the Hirnantian ice-sheet, that possibly reached 30° S [*Torsvik and Cocks*, 2013; *Pohl et al.*, 2016b], we impose a freshwater flux over a large area extending from 40° S to the South Pole (see insert in Fig. 9A). We run simulations for various values of the melt-water flux: 0.1, 0.5 and 1 Sv (1 Sv = $10^6$ $m^3.s^{-1}$). Although they are in the range that has usually been considered in water hosing experiments about the last glacial (e.g., *Prange et al.*, 2002 and *Stouffer et al.*, 2006; see discussion in *Roche et al.*, 2004), these levels of melt-water release are one or two orders of magnitude higher than the long-term average deduced from Hirnantian land-ice volume analysis. For instance, the eustatic curve reconstructed by *Loi et al.* [2010], using a backstripping procedure on the margin of Gondwana, shows a sea-level increase of ~ 70 m in 70 kyrs, equivalent to a melt-water flux of ~ 0.015 Sv in the Ordovician. Although sudden glacial outburst events would probably not be captured by *Loi et al.* [2010], our higher meltwater flux rate (1 Sv) is two orders of magnitude larger than the inferred average rate (0,015 Sv). Our simulations allow us to characterize the response (and potential recovery) of the early Silurian ocean to a weakening of the deep-water formation along the coast of Gondwana over a large range of meltwater fluxes.

Results are displayed in Fig. 9A. In the initial (undisturbed by freshwater) state (i.e., year 0 in Fig. 9A), two sites of particularly deep mixed layer stand out (red rectangles in Fig. 9C), with deep-water formation essentially occurring along the coast of Gondwana over the South Pole (region No. 1 in Fig. 9C, see also Fig. 4C). When a freshwater flux is imposed, the ocean circulation weakens, from an initial maximum (in absolute value) of ~ 25 Sv to ~ 24, 15 and 7 Sv after 500 years of perturbation with respectively 0.1, 0.5 and 1 Sv (Fig. 9A). A freshwater flux of 1 Sv, in particular, leads to a significant weakening of the circulation: the mixed layer gets shallower at site No. 2 and deep-water formation at site No. 1 virtually ceases (Fig. 9D), as testified by the lost of the Southern Hemisphere anticlockwise cell of the overturning circulation (compare Fig. 4C with Fig. 9B). Elsewhere, the structure of the

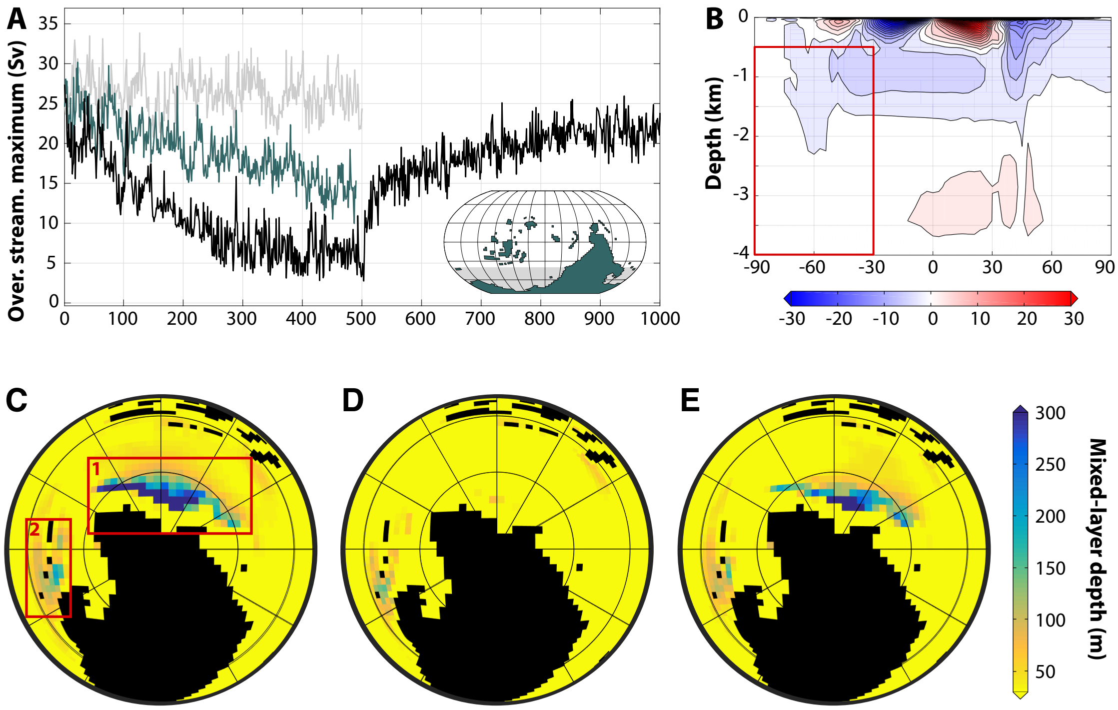


**Figure 9.** Results of the freshwater hosing experiments conducted at 345 W.m$^{-2}$. (**A**): Evolution of the intensity of the meridional overturning streamfunction as a function of model integration time for 3 values of imposed freshwater flux: 0.1 Sv (light grey line), 0.5 Sv (dark grey line) and 1 Sv (black line). The intensity of the streamfunction is computed, for each model year, as the maximum of the absolute value of the mean annual meridional streamfunction between 500 m depth and the ocean bottom, and between 90° S and 30° S (red rectangle in subplot **B**). The insert in the bottom-right corner represents the area over which the freshwater flux is applied. (**B**): Meridional overturning streamfunction averaged over the years 475 to 500 of the transient simulation with a flux of 1 Sv. The contour interval is 2.5 Sv. (**C**): Mixed-layer depth in the unperturbed steady-state (~ year 0 in subplot **A**). (**D**): Mixed-layer depth averaged over the years 475 to 500 of the transient simulation with 1 Sv. (**E**): Mixed-layer depth averaged over the years 975 to 1000 of the transient simulation with 1 Sv.

ocean circulation is unchanged. In particular, deep-water formation is not initiated elsewhere in response to the collapse of the Southern Hemisphere cell. When the freshwater flux is stopped the ocean circulation rapidly recovers, reaching 15 Sv after about 100 years (absolute value, see Fig. 9A). After 500 years, it almost reaches its initial intensity, and the two sites of deep-water formation reappear (Fig. 9E).

Previous water hosing experiments conducted under pre-industrial and last glacial conditions have shown that the initial climatic state may significantly impact the sensitivity of the climate system to a release of freshwater [*Ganopolski and Rahmstorf*, 2001; *Prange et al.*, 2002; *Kageyama et al.*, 2013]. In order to assess the robustness of our results under various climatic conditions, we repeat the freshwater hosing experiments under a warmer climate (350 $W.m^{-2}$, Fig. S8), and under an abrupt climate warming potentially representative of the Silurian deglaciation (Fig. S9). In both cases, the ocean circulation rapidly recovers when the release of melt water stops.

### 6.2 Impact of an increased nutrient supply to the ocean

Weathering of sediments exposed in formerly glaciated regions, promoted by global climate warming, may have favored the release of nutrients from the continents during the deglaciation [*Melchin et al.*, 2013]. This theory has been suggested in several published studies [e.g., *Armstrong et al.*, 2005, 2009; *Le Heron et al.*, 2013]. It is also supported by the changes in clay mineral composition documented in the Kufra basin (Libya) by *Meinhold et al.* [2015], who interpreted an increase in kaolinite content as probably representative of enhanced continental weathering due to the climate change occurring from the Late Ordovician icehouse to the Silurian greenhouse. Similarly, *Finlay et al.* [2010] demonstrated an increase in continental weathering concomitant with the deglaciation based on osmium isotope analysis. The possible diversification of non-vascular land plants during the Hirnantian [*Vecoli et al.*, 2011] – the weathering effect of which has been demonstrated [*Lenton et al.*, 2012; *Porada et al.*, 2016] – may also have constituted an additional source of nutrients to the ocean during the early Silurian deglaciation [*Melchin et al.*, 2013].

In this section, we therefore investigate the impact of an increased nutrient supply to the ocean on the marine primary productivity and oxygen concentration simulated in a warm climate (350 $W.m^{-2}$, see Sect. 3). A two-fold increase in continental weathering flux is easily reached under a warming climate [*Le Hir et al.*, 2009; *Beaulieu et al.*, 2012]. Once anoxic conditions are established, higher phosphate content can be further sustained through phosphorus regeneration from the sediment [*Van Cappellen and Ingall*, 1994; *Palastanga et al.*, 2011]. A first Silurian scenario considering an intensification of the continental weathering by a factor of 1.5 shows a strong increase in net primary productivity at the global scale (Fig. 10A). Levels of primary productivity allowing the deposition of black shales during the Katian (see Sect. 4, Fig. 3A in particular) are reached at all the localities reported by *Melchin et al.* [2013], except two of them found on the margin of Gondwana in the Paleo-Tethys. Based on the same criteria, a doubling nutrient supply provides a perfect model-data agreement (Fig. 10B). In detail, a doubling phosphate supply does not impact the values of surface primary productivity evenly in space, but induces significant changes in the spatial patterns (compare Fig. 11A with Fig. 3A). This is due to a large increase in the regions of previously minimum primary productivity (Fig. 11B), resulting from the saturating Michaelis-Menten kinetics used in the parametrization of NPP (Eq. 1). The maximal increase occurs in the area between eastern Baltica and western Gondwana, which was previously typified by oxic deposits during the Katian (Fig. 11B, see Sect. 4.1). As a consequence of the larger export of organic matter to depth, oxygen consumption by aerobic respiration gets more intense throughout the water column, and the oxygen concentration decreases in the ocean interior. At depth, the oxygen concentration decreases everywhere (Fig. 11C). The latter decrease is minimum in the cold waters over the North Pole (thermal effect), and in regions of deep water convection, which benefit from the input of oxygen-rich water masses coming from the surface ocean (ocean dynamics effect). The decrease in oxygen water content is maximum in the Paleo-Tethys, that does not benefit from any of these two effects and furthermore corresponds to the region of maximum increase in surface primary productivity (Fig. 11B). The impoverishment in dissolved oxygen is more moderate at the depth of the epicontinental seas because the exchange with the oxygen-rich mixed-layer waters is important (Fig. 11D). The largest decrease in oxygen content occurs with the upwelling of oxygen-depleted waters from the oxygen minimum zone, at equatorial latitudes and also in place of the Panthalassic Circumpolar Current in the Northern Hemisphere (Fig. 11D).

### 6.3 Discussion: the nutrient-driven Rhuddanian OAE

Two main arguments have been proposed to explain the early Rhuddanian OAE: release of melt water, salinity stratification and enhanced preservation of organic matter, or leaching of the newly-exposed glaciogenic sediments and nutrient-driven increase in ma-

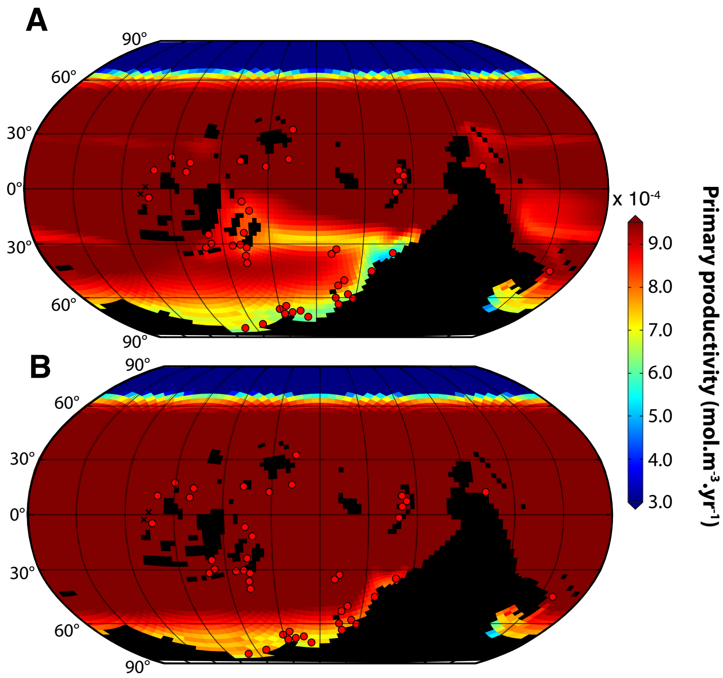


**Figure 10.** Surface primary productivity simulated using the 440 Ma land-sea mask, a solar forcing level of 350 W.m$^{-2}$ and an initial $PO_4$ depth profile defined as **(A)**: 1.5 times the values used in the baseline runs and **(B)**: 2 times the values used in the baseline runs. White and red dots respectively stand for sediments of early Silurian (Rhuddanian) age associated with dysoxic-to-oxic and at least intermittently anoxic conditions (i.e., interbedded black shales and black shales), after the compilation of *Melchin et al.* [2013]. See Fig. S2 for data points labeling. Same color scale as Fig. 3A.

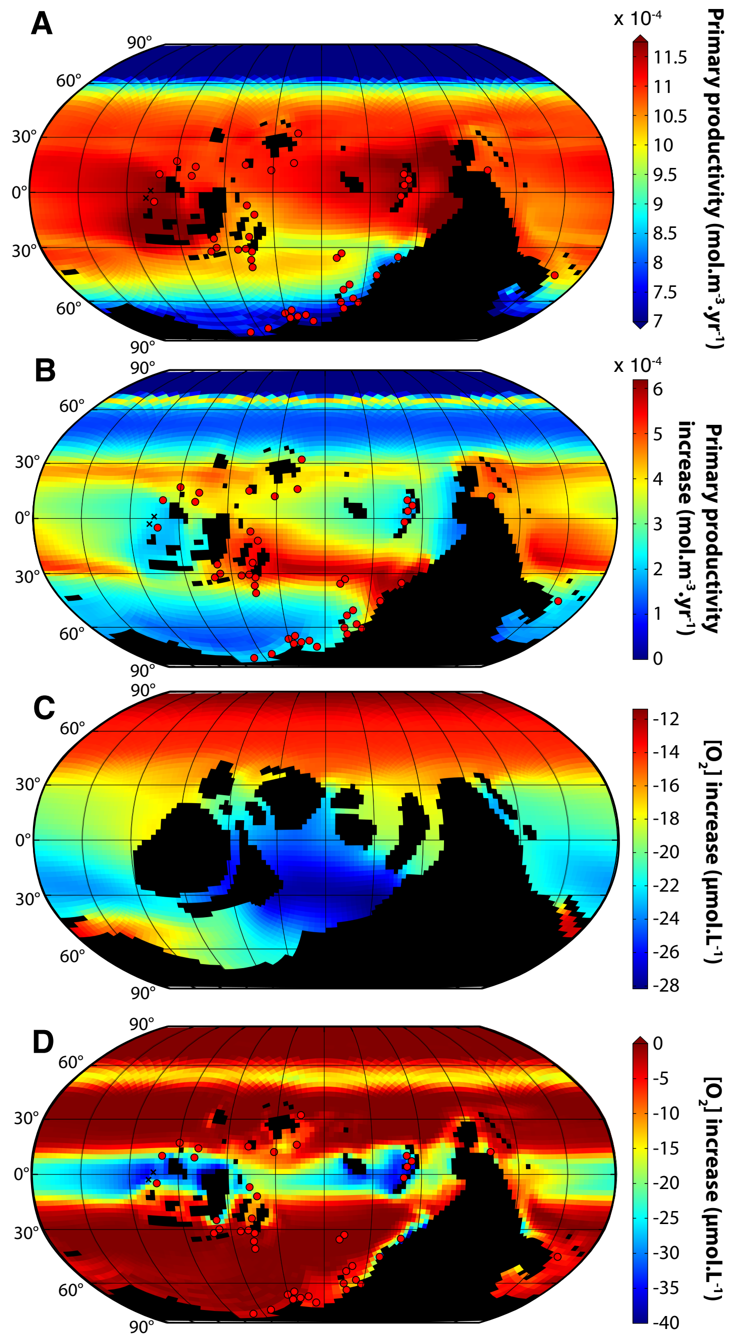


**Figure 11.** Impact of a doubling nutrient ($PO_4$) stock on the primary productivity simulated at the ocean surface, and on the oxygen concentration simulated throughout the water column. (**A**): Marine primary productivity simulated using the 440 Ma land-sea mask, a solar forcing level of 350 $W.m^{-2}$ and an initial $PO_4$ depth profile defined as twice the values used in the baseline runs. White and red dots after the compilation of *Melchin et al.* [2013]. Same as Fig. 10B, with better-suited color scale. (**B**): Increase in surface primary productivity simulated when doubling the nutrient stock in the ocean. (**C**): Increase in oxygen concentration simulated at the ocean bottom when doubling the initial ocean phosphate concentration. (**D**): Increase in oxygen concentration simulated at the depth of the epicontinental seas in the model ($\sim$ 80 m) when doubling the nutrient stock. The increase in oxygen concentration does not exceed 3.4 $\mu mol.L^{-1}$ anywhere.

rine primary productivity. We first investigated the "melt water hypothesis" by imposing a freshwater flux over the South Pole. Our simulations show that a limited water discharge (0.1 Sv) has virtually no effect on the ocean circulation. A strong freshwater flux (0.5 - 1 Sv) is required to induce the collapse of the latter. Such levels of water discharge over several thousands of years cannot be realistically maintained. For comparison, such rates have been associated with the melt-water pulses of the last glacial, and only over much shorter periods [e.g., *Prange et al.*, 2002]. The question however remains [e.g., *Melchin et al.*, 2013, p. 1659] whether abrupt events of this kind – of a few hundred of years in duration [*Roche et al.*, 2004] – could explain the deposition of black shales for several hundred thousand years in the early Silurian [*Armstrong et al.*, 2009; *Melchin et al.*, 2013]. In our model runs, the Ordovician overturning circulation rapidly collapses when a strong (1 Sv) freshwater flux is applied over the South Pole. However, once the flux is stopped, the ocean circulation promptly recovers, in a few hundred years as well, without showing any evidence of hysteresis. Although glacial outbursts have been documented during the demise of the Hirnantian ice-sheet, these events are supposed to have lasted several days to several years, with a 1-40 kyrs recurrence period [*Girard et al.*, 2012]. Therefore, such short-lived and occasional melt water pulses are no valid explanation for the protracted oxygen depletion event typifying the early Silurian ocean. We emphasize that some studies of the Last Glacial Maximum propose that, under certain conditions, the overturning circulation may not recover after a melt-water perturbation [*Prange et al.*, 2002]. This is not the case in our simulations with the Ordovician continental configuration. Our results suggest that the Late Ordovician-early Silurian ocean circulation is mono-stable, at least in the (large) range studied here. Taken as a whole, this suggests that the melt-water flux induced by the Late Ordovician deglaciation is unable to exert a persistent effect on the ocean circulation and thus on the ocean redox state at this time. Enhanced continental weathering constitutes the most probable driver for the Rhuddanian OAE, endorsing the visions that nutrient supply may constitute the dominant control on the spread of anoxia at various periods in the Earth's history [see *Monteiro et al.*, 2012]. Our results therefore support the theory developed by *Page et al.* [2007] regarding the long-term regulation of climate throughout the Early Paleozoic Ice Age. By favoring the sequestration of carbon in deep-sea sediments, post-glacial anoxia may have drawn down atmospheric $CO_2$ levels and thus acted as a negative feedback mechanism preventing the onset of runaway greenhouse conditions.

However, results of water-hosing experiments are model-dependent [*Stouffer et al.*, 2006; *Kageyama et al.*, 2013] and additional studies, in a warm climate, are needed before drawing definitive conclusions on the mechanisms that potentially caused anoxia in the early Silurian.

## 7 Model limitations and outlook

Modeling early Paleozoic climate and marine biogeochemistry involved some degree of simplification regarding the boundary conditions and the numerical model, which potentially affected our results. We discuss these limitations below in order to highlight key points that should be investigated in follow-up studies.

### 7.1 Simplified atmosphere

The main limitation of our numerical model is the highly simplified atmospheric component [SPEEDY, *Molteni*, 2003, see Sect. 2.1]. Given that the spatial distribution of simulated primary productivity essentially arises from the wind-driven ocean mixing processes (i.e., Ekman transport, Sect. 4.1), we pose the question: “Is our simplified atmospheric model able to correctly simulate wind stress at the surface of the Earth?" Despite the low vertical resolution of SPEEDY (5 layers), the annually-averaged wind stress simulated over the ocean is very similar to the one simulated using the FOAM model (Fig. S10). More importantly, the pattern of simulated NPP does not depend on the details of the surface winds, but on the existence of alternating bands of winds (i.e., Trades in the tropics, jet stream in the mid-latitudes, easterlies at high-latitudes). This feature is extremely robust across models, suggesting that the patterns of simulated primary productivity constitute a robust result of our study.

### 7.2 Boundary conditions: radiative forcing and flat bottom

Because the atmospheric component of our coupled model (SPEEDY) does not account for varying $p\mathrm{CO_2}$ levels, we simulated different climatic states by varying the solar forcing in the model (see Sect. 3.1). It has been demonstrated that a doubling $p\mathrm{CO_2}$ is equivalent to an increase by +3.7 W.m$^{-2}$ in the net downward radiation at the top of the atmosphere [*Myhre et al.*, 1998]. However, it has also been shown that changes in the solar irradiance and changes in atmospheric $\mathrm{CO_2}$ concentration that are equivalent from a purely radiative point of view do not produce identical climatic responses. A large part of the difference arises from the seasonal pattern of solar forcing, as opposed to greenhouse-gas forcing. *Lunt et al.* [2008] and *Schmidt et al.* [2012] notably simulated significantly different patterns of precipitation and atmospheric surface temperature while trying to compensate a 4-fold increase in $p\mathrm{CO_2}$ with decreased solar input. Since precipitation (through its impact on ocean salinity) and surface temperature are the two main drivers of the oceanic overturning circulation and thus deep ocean ventilation, it would be interesting to test the impact of a more "realistic" Ordovician forcing level [i.e., decreased solar luminosity, increased $p\mathrm{CO_2}$, see *Herrmann et al.*, 2003, 2004; *Pohl et al.*, 2014] on the oxygenation state of the ocean throughout the Ordovician-Silurian transition.

Similarly, we have not discussed the impact of the orbital configuration on simulated climate. By changing both the spatial and temporal distribution of the solar energy received at the surface of the Earth (for a given solar constant value), the orbital configuration may also have a strong climatic impact, potentially reinforced by the powerful sea-ice feedback. Unfortunately, the chaotic evolution of the orbits prevents a precise determination of the Earth motion beyond 65 Ma [*Laskar et al.*, 2004], so that no accurate orbital solution is available in the Ordovician. Future studies could address this issue through sensitivity tests to the orbital parameters (i.e., eccentricity, obliquity, precession).

In our study, we defined the Ordovician deep-ocean bathymetry as a flat bottom. We think that this constitutes the most conservative choice because the location and depth of early Paleozoic mid-ocean ridges is essentially speculative. Nonetheless, ocean ridges may alter our results. They could block deep-ocean currents and therefore promote isolation of ocean basins, while at the same time enhancing vertical mixing and topographic steering of the currents [e.g., *Gille et al.*, 2004]. These simultaneous, opposite effects make the overall ocean response difficult to predict. However, we do not think that the flat bottom constitutes a strong bias since several modeling studies on the Permian-Triassic boundary demonstrated a minor impact of ocean ridges on both the global large-scale ocean circulation and simulated bottom oxygen concentration [*Montenegro et al.*, 2011; *Osen et al.*, 2012].

### 7.3 Marine biogeochemistry

Our biogeochemistry submodel provided very new insights into the spatial distribution of primary productivity and dissolved oxygen concentration during the Ordovician. Still, some aspects of the modeling could be substantially improved.

First, no nutrient fluxes from the continent are used. A stock of phosphate is defined at the beginning of the simulation and riverine input is not considered. A direct consequence is that the flux of freshwater to the ocean provided by continental runoff dilutes ocean water in the model and therefore leads to a decrease in net primary productivity, whereas it could theoretically promote NPP through the input of erosion-derived nutrients. Second, sedimentation is not allowed in the model, precluding any explicit diagnostic of organic matter burial. Still, we realize that coupling a sediment model with a GCM is challenging. This would require specific modeling strategies such as asynchronous coupling methods in order to deal with the very long time constant associated with the sediments.

Here we simulated the changes in the patterns of potential Late Ordovician-early Silurian marine *biomass* productivity, in response to climate changes. The Ordovician-Silurian transition, however, is also characterized by fundamental turnovers in marine living communities (i.e., *biodiversity*), that may have regionally modulated the potential for surface primary productivity [e.g., *Kemp and Baldauf*, 1993] and thus massive organic matter burial [e.g., *Kemp et al.*, 1999]. Following the appearance of numerous phyla during the Cambrian Explosion [e.g., *Zhuravlev and Riding*, 2001], the Early and Middle Ordovician record their rapid diversification, at all taxonomic levels, during the “Great Ordovician Biodiversification Event" (GOBE, *Webby et al.*, 2004). This radiation is subsequently stopped by the Late Ordovician mass extinction, when ~ 85 % of all marine species disappear [*Sheehan*, 2001]. The Silurian eventually records a relatively rapid post-crisis recovery [*Servais et al.*, 2010]. The model employed in this study does not capture such variations in marine paleobiodiversity. Over the last decades, biogeochemistry models of the ocean continuously increased in complexity, by resolving more and more processes and by handling a growing number of species. Still, most up-to-date models only resolve a few phytoplankton functional types – such as diatoms, coccolithophores and nitrogen fixers – that correspond to aggregates of many modern species characterized by common biogeochemical requirements [e.g., *Aumont et al.*, 2015]. The physiological traits of these functional types are estimated from sensing, in-situ oceanic measurements, and laboratory culture experiments [*Anderson*, 2005]. In other words, these models are optimized for the present-day pelagic ecosystem, and cannot simulate the changes of the marine biodiversity seen in deep-time slices. However, recent developments in marine ecosystem models explore representations based on the principle that the community structure should self-organize, by selecting for phytoplankton with “fittest” physiological characteristics relative to surrounding environment [*Litchman et al.*, 2007; *Follows et al.*, 2007]. In this approach, tens or hundreds of phytoplankton types with various combinations of observation-based ecological strategies and physiological traits are carried in the model, and allowed to compete for the available resources. Such models mimic natural selection and satisfactorily simulate the first-order patterns of present-day marine biodiversity [e.g., *Barton et al.*, 2010]. We suggest that this kind of versatile marine ecology models may constitute suitable tools to further the present, exploratory study of the co-evolution of climate and the biosphere during the Early Paleozoic. This constitutes a future research target.

## 8 Conclusions

In this study, we employ an ocean-atmosphere setup of the MIT general circulation model (MITgcm) to investigate the changes in ocean redox state reported through the Ordovician-Silurian boundary. Our model accounts for marine primary productivity and cycling of oxygen in the ocean. We compare our modeling results with the recent black shale compilation of *Melchin et al.* [2013]. We show the following:

1. Under a warm climate representative of pre-Hirnantian times, our model does capture the spatial distribution of organic matter burial reported during the late Katian. Our results suggest that, under a reduced atmospheric oxygen partial pressure and thus reduced ocean oxygen content, the deposition of black shales in the Late Ordovician may have been driven by the patterns of surface primary productivity rather than deep-ocean oxygenation. We propose that the late Katian may therefore constitute an outstanding window into the Late Ordovician-early Silurian unperturbed oceanic redox state, and that any deviation from this should be considered as evidence of climatic perturbation or specific basinal conditions and insulation from the open-ocean.
2. When a climate cooling is applied, combined effects of preferential oxygen dissolution in cold waters and enhanced oceanic overturning induce a significant oxygenation throughout the water column, providing support for an “Hirnantian oxygenation event". These results contrast with some recent studies invoking an Hirnantian deep-water anoxic event to resolve both the positive carbon excursion reported at this time, through massive organic carbon burial, and the concomitant Late Ordovician mass extinction, through the release of toxic metals under suboxic conditions. If evidence of deep-water anoxia during the Hirnantian should be discovered in the future [*Vandenbroucke et al.*, 2015], mechanisms other than climate cooling should obviously be in-

voked to explain it. Such mechanisms should have a large enough effect to overcome the increased solubility.

3. In our model runs, the input of freshwater over the South Pole is not able to sustain a state of low oceanic ventilation over sufficiently long geological periods to produce the record of early Silurian anoxia. Enhanced continental weathering and nutrient input to the ocean satisfactorily account for the preferential deposition of black shales at that time.

## Acknowledgements

The findings in this study are based on climatic fields simulated by the ocean-atmosphere general circulation model MITgcm. Code for the climate model MITgcm can be accessed at http://mitgcm.org. Requests for the climate model output can be sent to A.P (pohl@cerege.fr) or Y.D. (donnadieu@cerege.fr). The authors acknowledge the financial support from the CNRS (INSU, action SYSTER). A.P. and Y.D. thank the CEA/CCRT for providing access to the HPC resources of TGCC under the allocation 2014-012212 made by GENCI. A.P. thanks Maura Brunetti from the University of Geneva, who provided expertise that greatly assisted the research. The authors also want to thank the two anonymous reviewers of this manuscript and associate editor Gabe Bowen for their helpful and constructive comments and suggestions, and Ellen Thomas for editorial handling. This research was funded through a CEA PhD grant CFR. This is a contribution to the IGCP Project-591, "The Early to Middle Paleozoic Revolution" and IGCP Project-653, "The onset of the Great Ordovician Biodiversity Event".

## References

Adcroft, A., C. Hill, and J. Marshall (1997), Representation of topography by shaved cells in a height coordinate ocean model, *Monthly Weather Review*, *125*, 2293–2315.

Adcroft, A., J. M. Campin, and C. Hill (2004), Implementation of an atmosphere-ocean general circulation model on the expanded spherical cube, *Monthly Weather Review*, *132*, 2845–2863.

Algeo, T. J., and E. Ingall (2007), Sedimentary $C_{org}$:P ratios, paleocean ventilation, and Phanerozoic atmospheric $pO_2$, *Palaeogeography, palaeoclimatology, palaeoecology*, *256*(3-4), 130–155.

Algeo, T. J., and J. B. Maynard (2008), Trace-metal covariation as a guide to water-mass conditions in ancient anoxic marine environments, *Geosphere*, *4*(5), 872.

Anderson, T. R. (2005), Plankton functional type modelling: running before we can walk?, *Journal of Plankton Research*, *27*(11), 1073–1081.

Armstrong, H. A., and A. L. Coe (1997), Deep-sea sediments record the geophysiology of the late Ordovician glaciation, *Journal of the Geological Society of London*, *154*, 929–934.

Armstrong, H. A., B. R. Turner, I. M. Makhlouf, G. P. Weedon, M. Williams, A. Al Smadi, and A. Abu Salah (2005), Origin, sequence stratigraphy and depositional environment of an upper Ordovician (Hirnantian) deglacial black shale, Jordan, *Palaeogeography, palaeoclimatology, palaeoecology*, *220*(3-4), 273–289.

Armstrong, H. A., G. D. Abbott, B. R. Turner, I. M. Makhlouf, A. B. Muhammad, N. Pedentchouk, and H. Peters (2009), Black shale deposition in an Upper Ordovician–Silurian permanently stratified, peri-glacial basin, southern Jordan, *Palaeogeography, palaeoclimatology, palaeoecology*, *273*(3-4), 368–377.

Arthur, M. A. (1979), North Atlantic Cretaceous black shales: the record at site 398 and a brief comparison with other occurences, in *Initial Rep. Deep Sea*, edited by J. C. Sibuet, W. B. F. Ryan, M. A. Arthur, R. O. Barnes, D. Habib, S. Iaccarino, D. Johnson, B. Lopatin, A. Maldonado, D. G. Moore, G. E. Morgan, J.-P. Réhault, J. Sigal, and C. A. Williams, pp. 719–751, US Government Printing Office, Washington.

Aumont, O., C. Ethé, A. Tagliabue, L. Bopp, and M. Gehlen (2015), PISCES-v2: an ocean biogeochemical model for carbon and ecosystem studies, *Geoscientific Model Development*, *8*(8), 2465–2513.

Barton, A. D., S. Dutkiewicz, G. Flierl, J. Bragg, and M. J. Follows (2010), Patterns of diversity in marine phytoplankton, *Science*, *327*(5972), 1509–1511.

Beaulieu, E., Y. Goddéris, Y. Donnadieu, D. Labat, and C. Roelandt (2012), High sensitivity of the continental-weathering carbon dioxide sink to future climate change, *Nature Climate Change*, *2*(5), 346–349.

Bergman, N. M., T. M. Lenton, and A. J. Watson (2004), COPSE: A new model of biogeochemical cycling over Phanerozoic time, *American Journal of Science*, *304*, 397–437.

Berner, R. A. (2006), GEOCARBSULF: A combined model for Phanerozoic atmospheric $O_2$ and $CO_2$, *Geochimica et Cosmochimica Acta*, *70*(23), 5653–5664.

Berner, R. A. (2009), Phanerozoic atmospheric oxygen: New results using the GEOCARBSULF model, *American Journal of Science*, *309*, 603–606.

Berry, W. B. N., P. Wilde, and M. S. Quinby-Hunt (1990), Late Ordovician graptolite mass mortality and subsequent early silurian re-radiation, in *Lecture Notes in Earth Sciences*, pp. 115–123, Springer, Berlin/Heidelberg.

Bickert, T., J. Pätzold, C. Samtleben, and A. Munnecke (1997), Paleoenvironmental changes in the Silurian indicated by stable isotopes in brachiopod shells from Gotland, Sweden, *Geochimica et Cosmochimica Acta*, *61*(13), 2717–2730.

Blakey, R. C. (2016), Colorado Plateau Geosystems [http://cpgeosystems.com].

Brenchley, P. J., J. D. Marshall, G. Carden, D. Robertson, D. Long, T. Meidla, L. Hints, and T. F. Anderson (1994), Bathymetric and isotopic evidence for a short-lived Late Ordovician glaciation in a greenhouse period, *Geology*, *22*(4), 295–298.

Brenchley, P. J., G. Carden, and J. Marshall (1995), *Environmental changes associated with the" first strike" of the Late Ordovician mass extinction*, vol. 20, Modern Geology.

Brenchley, P. J., G. A. Carden, L. Hints, D. Kaljo, J. D. Marshall, T. Martma, T. Meidla, and J. Nõlvak (2003), High-resolution stable isotope stratigraphy of Upper Ordovician sequences: Constraints on the timing of bioevents and environmental changes associated with mass extinction and glaciation, *Geological Society of America Bulletin*, *115*(1), 89–104.

Brunetti, M., C. Vérard, and P. O. Baumgartner (2015), Modeling the Middle Jurassic ocean circulation, *Journal of Palaeogeography*, *4*(4), 371–383.

Bryant, R. G. (2013), Recent advances in our understanding of dust source emission processes, *Progress in Physical Geography*, *37*(3), 397–421.

Came, R. E., J. M. Eiler, J. Veizer, K. Azmy, U. Brand, and C. R. Weidman (2007), Coupling of surface temperatures and atmospheric $CO_2$ concentrations during the Palaeozoic era, *Nature*, *449*, 198–202.

Chaloner, W. G. (1989), Fossil charcoal as an indicator of palaeoatmospheric oxygen level, *Journal of the Geological Society*, *146*(1), 171–174.

Cocks, L. R. M., and T. H. Torsvik (2005), Baltica from the late Precambrian to mid-Palaeozoic times: The gain and loss of a terrane's identity, *Earth-Science Reviews*, *72*(1-2), 39–66.

Cocks, L. R. M., and T. H. Torsvik (2007), Siberia, the wandering northern terrane, and its changing geography through the Palaeozoic, *Earth-Science Reviews*, *82*(1-2), 29–74.

Cocks, L. R. M., and T. H. Torsvik (2011), The Palaeozoic geography of Laurentia and western Laurussia: A stable craton with mobile margins, *Earth-Science Reviews*, *106*(1-2), 1–51.

Cocks, L. R. M., and T. H. Torsvik (2013), The dynamic evolution of the Palaeozoic geography of eastern Asia, *Earth-Science Reviews*, *117*(C), 40–79.

Cramer, B. D., and M. R. Saltzman (2005), Sequestration of $^{12}$C in the deep ocean during the early Wenlock (Silurian) positive carbon isotope excursion, *Palaeogeography, palaeoclimatology, palaeoecology*, *219*(3-4), 333–349.

Cramer, B. D., and M. R. Saltzman (2007a), Fluctuations in epeiric sea carbonate production during Silurian positive carbon isotope excursions: A review of proposed paleoceanographic models, *Palaeogeography, palaeoclimatology, palaeoecology*, *245*(1-2), 37–45.

Cramer, B. D., and M. R. Saltzman (2007b), Early Silurian paired $\delta^{13}C_{carb}$ and $\delta^{13}C_{org}$ analyses from the Midcontinent of North America: Implications for paleoceanography and paleoclimate, *Palaeogeography, palaeoclimatology, palaeoecology*, *256*(3-4), 195–203.

Denis, M., J.-F. Buoncristiani, M. Konaté, J.-F. Ghienne, and M. Guiraud (2007), Hirnantian glacial and deglacial record in SW Djado Basin (NE Niger), *Geodinamica Acta*, *20*(3), 177–195.

Donnadieu, Y., E. Pucéat, M. Moiroud, F. Guillocheau, and J.-F. Deconinck (2016), A better-ventilated ocean triggered by Late Cretaceous changes in continental configuration, *Nature communications*, *7*, 10,316.

Dutkiewicz, S., M. J. Follows, and P. Parekh (2005), Interactions of the iron and phosphorus cycles: A three-dimensional model study, *Global Biogeochemical Cycles*, *19*(1), GB1021.

Edwards, D., L. Cherns, and J. A. Raven (2015), Could land-based early photosynthesizing ecosystems have bioengineered the planet in mid-Palaeozoic times?, *Palaeontology*, *58*(5), 803–837.

Ekman, V. W. (1905), On the influence of the earth's rotation on ocean currents, *Ark. Mat. Astron. Fys.*, *2*, 1–53.

Enderton, D. (2009), On the meridional heat transport and its partition between the atmosphere and oceans, Ph.D. thesis, Massachusetts Institute of Technology.

Enderton, D., and J. Marshall (2009), Explorations of atmosphere–ocean–ice climates on an aquaplanet and their meridional energy transports, *Journal of the Atmospheric Sciences*, *66*(6), 1593–1611.

Falkowski, P. (2012), Ocean science: the power of plankton., *Nature*, *483*(7387), S17–S20.

Ferreira, D., J. Marshall, and J.-M. Campin (2010), Localization of deep water formation: role of atmospheric moisture transport and geometrical constraints on ocean circulation, *Journal of Climate*, *23*(6), 1456–1476.

Ferreira, D., J. Marshall, and B. Rose (2011), Climate determinism revisited: multiple equilibria in a complex climate model, *Journal of Climate*, *24*(4), 992–1012.

Finlay, A. J., D. Selby, and D. R. Gröcke (2010), Tracking the Hirnantian glaciation using Os isotopes, *Earth and Planetary Science Letters*, *293*(3-4), 339–348.

Finnegan, S., K. Bergmann, J. M. Eiler, D. S. Jones, D. A. Fike, I. Eisenman, N. C. Hughes, A. K. Tripati, and W. W. Fischer (2011), The magnitude and duration of Late Ordovician-Early Silurian glaciation, *Science*, *331*(6019), 903–906.

Finney, S. C., W. Berry, J. D. Cooper, and R. L. Ripperdan (1999), Late Ordovician mass extinction: A new perspective from stratigraphic sections in central Nevada, *Geology*, *27*(3), 215–218.

Follows, M. J., S. Dutkiewicz, S. Grant, and S. W. Chisholm (2007), Emergent biogeography of microbial communities in a model ocean, *Science*, *315*(5820), 1843–1846.

Friis, K., R. G. Najjar, M. J. Follows, and S. Dutkiewicz (2006), Possible overestimation of shallow-depth calcium carbonate dissolution in the ocean, *Global Biogeochemical Cycles*, *20*(4), GB4019.

Friis, K., R. G. Najjar, M. J. Follows, S. Dutkiewicz, A. Körtzinger, and M. Johnson (2007), Dissolution of calcium carbonate: observations and model results in the subpolar North Atlantic, *Biogeosciences*, *4*, 205–213.

Ganopolski, A., and S. Rahmstorf (2001), Rapid changes of glacial climate simulated in a coupled climate model, *Nature*, *409*(6817), 153–158.

Garcia, H. E., and L. I. Gordon (1992), Oxygen solubility in seawater: Better fitting equations, *Limnology and Oceanography*, *37*(6), 1307–1312.

Gent, P. R., and J. C. McWilliams (1990), Isopycnal mixing in ocean circulation models, *Journal of Physical Oceanography*, *20*, 150–155.

Ghienne, J.-F., D. P. Le Heron, J. Moreau, M. Denis, and M. Deynoux (2007), The Late Ordovician glacial sedimentary system of the North Gondwana platform, in *Glacial Sedimentary Processes and Products, Special Publication*, edited by M. Hambrey, P. Christoffersen, N. Glasser, P. Janssen, B. Hubbard, and M. Siegert, pp. 295–319, International Association of Sedimentologists, Blackwells, Oxford.

Gille, S. T., E. J. Metzger, and R. Tokmakian (2004), Seafloor topography and ocean circulation, *Oceanography*, *17*(1), 47–54.

Girard, F., J.-F. Ghienne, and J.-L. Rubino (2012), Occurrence of hyperpycnal flows and hybrid event beds related to glacial outburst events in a Late Ordovician proglacial delta (Murzuq Basin, SW Libya), *Journal of Sedimentary Research*, *82*(9), 688–708.

Hammarlund, E. U., T. W. Dahl, D. A. T. Harper, D. P. G. Bond, A. T. Nielsen, C. J. Bjerrum, N. H. Schovsbo, H. P. Schönlaub, J. A. Zalasiewicz, and D. E. Canfield (2012), A sulfidic driver for the end-Ordovician mass extinction, *Earth and Planetary Science Letters*, *331-332*(C), 128–139.

Haq, B. U., and S. R. Schutter (2008), A chronology of Paleozoic sea-level changes, *Science*, *322*(5898), 64–68.

Harper, D. A. T., E. U. Hammarlund, and C. M. Ø. Rasmussen (2013a), End Ordovician extinctions: A coincidence of causes, *Gondwana Research*, *25*(4), 1294–1307.

Harper, D. A. T., C. M. O. Rasmussen, M. Liljeroth, R. B. Blodgett, Y. Candela, J. Jin, I. G. Percival, J. y. Rong, E. Villas, and R. b. Zhan (2013b), Biodiversity, biogeography and phylogeography of Ordovician rhynchonelliform brachiopods, in *Early Palaeozoic biogeography and palaeogeography*, edited by D. A. T. Harper and T. Servais, pp. 127–144, Geological Society of London, Memoirs.

Heckman, D. S., D. M. Geiser, B. R. Eidell, and R. L. Stauffer (2001), Molecular evidence for the early colonization of land by fungi and plants, *Science*, *293*, 1129–1133.

Herrmann, A. D., M. E. Patzkowsky, and D. Pollard (2003), Obliquity forcing with 8–12 times preindustrial levels of atmospheric $p\mathrm{CO_2}$ during the Late Ordovician glaciation, *Geology*, *31*(6), 485–488.

Herrmann, A. D., B. J. Haupt, M. E. Patzkowsky, D. Seidov, and R. L. Slingerland (2004), Response of Late Ordovician paleoceanography to changes in sea level, continental drift, and atmospheric $p\mathrm{CO_2}$: potential causes for long-term cooling and glaciation, *Palaeo-*

*geography, palaeoclimatology, palaeoecology*, *210*(2-4), 385–401.

Hoffman, D. L., T. J. Algeo, J. B. Maynard, M. M. Joachimski, J. C. Hower, and J. Jaminski (1998), Regional and stratigraphic variation in bottomwater anoxia in offshore core shales of Upper Pennsylvanian cyclothems from the Eastern Midcontinent Shelf (Kansas), U.S.A., in *Shales and Mudstones I*, edited by J. Schieber, pp. 243–269, Schweizerbart'sche Verlagsbuchhandlung, Stuttgart.

Jacob, R. L. (1997), Low frequency variability in a simulated atmosphere ocean system, Ph.D. thesis, University of Wisconsin-Madison.

Jenkyns, H. C. (2010), Geochemistry of oceanic anoxic events, *Geochemistry, Geophysics, Geosystems*, *11*(3), Q03,004.

Jeppsson, L. (1990), An oceanic model for lithological and faunal changes tested on the Silurian record, *Journal of the Geological Society*, *147*(4), 663–674.

Johnson, M. E. (2006), Relationship of Silurian sea-level fluctuations to oceanic episodes and events, *GFF*, *128*(2), 115–121.

Jones, D. S., and D. A. Fike (2013), Dynamic sulfur and carbon cycling through the end-Ordovician extinction revealed by paired sulfate–pyrite $\delta^{34}$S, *Earth and Planetary Science Letters*, *363*, 144–155.

Kageyama, M., U. Merkel, B. Otto-Bliesner, M. Prange, A. Abe-Ouchi, G. Lohmann, R. Ohgaito, D. M. Roche, J. Singarayer, D. Swingedouw, and X. Zhang (2013), Climatic impacts of fresh water hosing under Last Glacial Maximum conditions: a multi-model study, *Climate of the Past*, *9*(2), 935–953.

Kaljo, D., T. Martma, P. Männik, and V. Viira (2003), Implications of Gondwana glaciations in the Baltic late Ordovician and Silurian and a carbon isotopic test of environmental cyclicity, *Bulletin de la Société géologique de France*, *174*(1), 59–66.

Kemp, A., and J. G. Baldauf (1993), Vast Neogene laminated diatom mat deposits from the eastern equatorial Pacific Ocean, *Nature*, *362*, 141–144.

Kemp, A., R. B. Pearce, I. Koizumi, J. Pike, and S. J. Rance (1999), The role of mat-forming diatoms in the formation of Mediterranean sapropels, *Nature*, *399*, 57–60.

Kump, L. R., M. A. Arthur, M. E. Patzkowsky, M. T. Gibbs, D. S. Pinkus, and P. M. Sheehan (1999), A weathering hypothesis for glaciation at high atmospheric $p\mathrm{CO}_2$ during the Late Ordovician, *Palaeogeography, palaeoclimatology, palaeoecology*, *152*(1), 173–187.

LaPorte, D. F., C. Holmden, W. P. Patterson, J. D. Loxton, M. J. Melchin, C. E. Mitchell, S. C. Finney, and H. D. Sheets (2009), Local and global perspectives on carbon and nitrogen cycling during the Hirnantian glaciation, *Palaeogeography, palaeoclimatology, palaeoecology*, *276*(1-4), 182–195.

Large, W. G., J. C. McWilliams, and S. C. Doney (1994), Oceanic vertical mixing: a review and a model with a nonlocal boundary layer parameterization, *Reviews of Geophysics*, *32*(4), 363–403.

Laskar, J., P. Robutel, F. Joutel, M. Gastineau, A. Correia, and B. Levrard (2004), A long-term numerical solution for the insolation quantities of the Earth, *Astronomy & Astrophysics*, *428*(1), 261–285.

Le Heron, D. P., and J. Craig (2008), First-order reconstructions of a Late Ordovician Saharan ice sheet, *Journal of the Geological Society of London*, *165*, 19–29.

Le Heron, D. P., and J. A. Dowdeswell (2009), Calculating ice volumes and ice flux to constrain the dimensions of a 440 Ma North African ice sheet, *Journal of the Geological Society*, *166*(2), 277–281.

Le Heron, D. P., J. Craig, and J. L. Etienne (2009), Ancient glaciations and hydrocarbon accumulations in North Africa and the Middle East, *Earth-Science Reviews*, *93*(3-4), 47–76.

Le Heron, D. P., G. Meinhold, A. Page, and A. Whitham (2013), Did lingering ice sheets moderate anoxia in the Early Palaeozoic of Libya?, *Journal of the Geological Society*, *170*(2), 327–339.

Le Hir, G., Y. Donnadieu, Y. Goddéris, R. T. Pierrehumbert, G. P. Halverson, M. Macouin, A. Nédélec, and G. Ramstein (2009), The snowball Earth aftermath: Exploring the limits of continental weathering processes, *Earth and Planetary Science Letters*, *277*(3-4), 453–463.

Lenton, T. M., M. Crouch, M. Johnson, N. Pires, and L. Dolan (2012), First plants cooled the Ordovician, *Nature Geoscience*, *5*(2), 86–89.

Lenton, T. M., T. W. Dahl, S. J. Daines, B. J. W. Mills, K. Ozaki, M. R. Saltzman, and P. Porada (2016), Earliest land plants created modern levels of atmospheric oxygen, *Proceedings of the National Academy of Sciences of the United States of America*, p. 201604787.

Litchman, E., C. A. Klausmeier, O. M. Schofield, and P. G. Falkowski (2007), The role of functional traits and trade-offs in structuring phytoplankton communities: scaling from cellular to ecosystem level, *Ecology Letters*, *10*(12), 1170–1181.

Loi, A., J.-F. Ghienne, M. P. Dabard, F. Paris, A. Botquelen, N. Christ, Z. Elaouad-Debbaj, A. Gorini, M. Vidal, B. Videt, and J. Destombes (2010), The Late Ordovician glacio-eustatic record from a high-latitude storm-dominated shelf succession: The Bou Ingarf section (Anti-Atlas, Southern Morocco), *Palaeogeography, palaeoclimatology, palaeoecology*, *296*(3-4), 332–358.

Long, D. (1993), Oxygen and carbon isotopes and event stratigraphy near the Ordovician–Silurian boundary, Anticosti Island Quebec, *Palaeogeography, palaeoclimatology, palaeoecology*, *104*, 49–59.

Loydell, D. K. (2007), Early Silurian positive $\delta^{13}$C excursions and their relationship to glaciations, sea-level changes and extinction events, *Geological Journal*, *42*(5), 531–546.

Loydell, D. K. (2008), Reply to 'Early Silurian positive $\delta^{13}$C excursions and their relationship to glaciations, sea-level changes and extinction events: discussion' by Bradley D. Cramer and Axel Munnecke, *Geological Journal*, *43*(4), 511–515.

Lunt, D. J., A. Ridgwell, P. J. Valdes, and A. Seale (2008), "Sunshade World": A fully coupled GCM evaluation of the climatic impacts of geoengineering, *Geophysical Research Letters*, *35*(12), L12,710.

Luo, G., T. J. Algeo, R. Zhan, D. Yan, J. Huang, J. Liu, and S. Xie (2016), Perturbation of the marine nitrogen cycle during the Late Ordovician glaciation and mass extinction, *Palaeogeography, palaeoclimatology, palaeoecology*, *448*, 339–348.

Marshall, J., and K. Speer (2012), Closure of the meridional overturning circulation through Southern Ocean upwelling, *Nature Geoscience*, *5*(3), 171–180.

Marshall, J., A. Adcroft, C. Hill, L. Perelman, and C. Heisey (1997a), A finite-volume, incompressible Navier Stokes model for studies of the ocean on parallel computers, *Journal of Geophysical Research*, *102*(C3), 5753–5766.

Marshall, J., C. Hill, L. Perelman, and A. Adcroft (1997b), Hydrostatic, quasi-hydrostatic, and nonhydrostatic ocean modeling, *Journal of Geophysical Research*, *102*(C3), 5733–5752.

Marshall, J., A. Adcroft, J. M. Campin, C. Hill, and A. White (2004), Atmosphere-ocean modeling exploiting fluid isomorphisms, *Monthly Weather Review*, *132*, 2882–2894.

Marshall, J., D. Ferreira, J. M. Campin, and D. Enderton (2007), Mean climate and variability of the atmosphere and ocean on an aquaplanet, *Journal of the Atmospheric Sciences*, *64*(12), 4270–4286.

Martin, J. H., G. A. Knauer, D. M. Karl, and W. W. Broenkow (1987), VERTEX: carbon cycling in the northeast Pacific, *Deep Sea Research*, *34*(2), 267–285.

McKinley, G. A., M. J. Follows, and J. Marshall (2004), Mechanisms of air-sea $CO_2$ flux variability in the equatorial Pacific and the North Atlantic, *Global Biogeochemical Cycles*, *18*(2), GB2011.

Meinhold, G., D. P. Le Heron, M. Elgadry, and Y. Abutarruma (2015), The search for 'hot shales' in the western Kufra Basin, Libya: geochemical and mineralogical characterisation of outcrops, and insights into latest Ordovician climate, *Arabian Journal of Geosciences*, *9*(1), 62.

Melchin, M. J., C. E. Mitchell, C. Holmden, and P. Štorch (2013), Environmental changes in the Late Ordovician-early Silurian: Review and new insights from black shales and nitrogen isotopes, *Geological Society of America Bulletin*, *125*(11-12), 1635–1670.

Molteni, F. (2003), Atmospheric simulations using a GCM with simplified physical parametrizations. I: Model climatology and variability in multi-decadal experiments, *Climate Dynamics*, *20*(2-3), 175–191.

Monteiro, F. M., R. D. Pancost, A. Ridgwell, and Y. Donnadieu (2012), Nutrients as the dominant control on the spread of anoxia and euxinia across the Cenomanian-Turonian oceanic anoxic event (OAE2): Model-data comparison, *Paleoceanography*, *27*(4), PA4209.

Montenegro, A., P. Spence, K. J. Meissner, M. Eby, M. J. Melchin, and S. T. Johnston (2011), Climate simulations of the Permian-Triassic boundary: Ocean acidification and the extinction event, *Paleoceanography*, *26*(3), PA3207.

Moreau, J. (2011), The Late Ordovician deglaciation sequence of the SW Murzuq Basin (Libya), *Basin Research*, *23*(4), 449–477.

Munnecke, A., M. Calner, D. A. T. Harper, and T. Servais (2010), Ordovician and Silurian sea–water chemistry, sea level, and climate: A synopsis, *Palaeogeography, palaeoclimatology, palaeoecology*, *296*(3-4), 389–413.

Myhre, G., E. J. Highwood, K. P. Shine, and F. Stordal (1998), New estimates of radiative forcing due to well mixed greenhouse gases, *Geophysical Research Letters*, *25*(14), 2715–2718.

Nardin, E., Y. Goddéris, Y. Donnadieu, G. Le Hir, R. C. Blakey, E. Pucéat, and M. Aretz (2011), Modeling the early Paleozoic long-term climatic trend, *Geological Society of America Bulletin*, *123*(5-6), 1181–1192.

Och, L. M., L. Cremonese, G. A. Shields-Zhou, S. W. Poulton, U. Struck, H. Ling, D. Li, X. Chen, C. Manning, M. Thirlwall, H. Strauss, and M. Zhu (2015), Palaeoceanographic controls on spatial redox distribution over the Yangtze Platform during the Ediacaran-Cambrian transition, *Sedimentology*, *63*(2), 378–410.

Osen, A. K., A. M. E. Winguth, C. Winguth, and C. R. Scotese (2012), Sensitivity of Late Permian climate to bathymetric features and implications for the mass extinction, *Global and Planetary Change*, pp. 171–179.

Owens, J. D., T. W. Lyons, D. S. Hardisty, C. M. Lowery, Z. Lu, B. Lee, and H. C. Jenkyns (2017), Patterns of local and global redox variability during the Cenomanian-Turonian Boundary Event (Oceanic Anoxic Event 2) recorded in carbonates and shales from central Italy, *Sedimentology*, *64*(1), 168–185.

Page, A., J. A. Zalasiewicz, M. Williams, and L. E. Popov (2007), Were transgressive black shales a negative feedback modulating glacioeustasy in the Early Palaeozoic Icehouse?, in *Deep-Time Perspectives on Climate Change: Marrying the Signal from Computer Models and Biological Proxies*, edited by M. Williams, A. M. Haywood, F. J. Gregory, and D. N. Schmidt, pp. 123–156, The Micropalaeontological Society, Special Publications. The Geological Society, London.

Palastanga, V., C. P. Slomp, and C. Heinze (2011), Long-term controls on ocean phosphorus and oxygen in a global biogeochemical model, *Global Biogeochemical Cycles*, *25*(3), GB3024.

Pohl, A., Y. Donnadieu, G. Le Hir, J. F. Buoncristiani, and E. Vennin (2014), Effect of the Ordovician paleogeography on the (in)stability of the climate, *Climate of the Past*, *10*(6), 2053–2066.

Pohl, A., E. Nardin, T. Vandenbroucke, and Y. Donnadieu (2016a), High dependence of Ordovician ocean surface circulation on atmospheric $CO_2$ levels, *Palaeogeography, palaeoclimatology, palaeoecology*, *458*, 39–51.

Pohl, A., Y. Donnadieu, G. Le Hir, J. B. Ladant, C. Dumas, J. Alvarez-Solas, and T. R. A. Vandenbroucke (2016b), Glacial onset predated Late Ordovician climate cooling, *Paleoceanography*, *31*, 800–821.

Porada, P., T. M. Lenton, A. Pohl, B. Weber, L. Mander, Y. Donnadieu, C. Beer, U. Pöschl, and A. Kleidon (2016), High potential for weathering and climate effects of non-vascular vegetation in the Late Ordovician, *Nature communications*, *7*, 12,113.

Poulsen, C. J., C. Tabor, and J. D. White (2015), Long-term climate forcing by atmospheric oxygen concentrations, *Science*, *348*(6240), 1238–1241.

Poussart, P. F., A. J. Weaver, and C. R. Barnes (1999), Late Ordovician glaciation under high atmospheric $CO_2$: A coupled model analysis, *Paleoceanography*, *14*(4), 542–558.

Prange, M., V. Romanova, and G. Lohmann (2002), The glacial thermohaline circulation: Stable or unstable?, *Geophysical Research Letters*, *29*(21), 2028.

R Core Team (2013), R: A Language and Environment for Statistical Computing.

Rahmstorf, S. (1996), On the freshwater forcing and transport of the Atlantic thermohaline circulation, *Climate Dynamics*, *12*, 799–811.

Rasmussen, C. M. Ø., and D. A. T. Harper (2011), Did the amalgamation of continents drive the end Ordovician mass extinctions?, *Palaeogeography, palaeoclimatology, palaeoecology*, *311*(1-2), 48–62.

Redi, M. H. (1982), Oceanic isopycnal mixing by coordinate rotation, *Journal of Physical Oceanography*, *12*, 1154–1158.

Roche, D., D. Paillard, and E. Cortijo (2004), Constraints on the duration and freshwater release of Heinrich event 4 through isotope modelling, *Nature*, *432*(7015), 379–382.

Roche, D. M., A. P. Wiersma, and H. Renssen (2009), A systematic study of the impact of freshwater pulses with respect to different geographical locations, *Climate Dynamics*, *34*(7-8), 997–1013.

Rose, B. E. J., and J. Marshall (2009), Ocean heat transport, sea ice, and multiple climate states: Insights from energy balance models, *Journal of the Atmospheric Sciences*, *66*(9), 2828–2843.

Rubinstein, C. V., P. Gerrienne, G. S. de la Puente, R. A. Astini, and P. Steemans (2010), Early Middle Ordovician evidence for land plants in Argentina (eastern Gondwana), *New Phytologist*, *188*(2), 365–369.

Ruttenberg, K. C. (1993), Reassessment of the oceanic residence time of phosphorus, *Chemical Geology*, *107*, 405–409.

Sageman, B. B., S. R. Meyers, and M. A. Arthur (2006), Orbital time scale and new C-isotope record for Cenomanian-Turonian boundary stratotype, *Geology*, *34*(2), 125–128.

Schlanger, S. O., and H. C. Jenkyns (2007), Cretaceous oceanic anoxic events: causes and consequences, *Geologie en Mijnbouw*, *55*(4-3), 179–184.

Schmidt, H., K. Alterskjær, D. Bou Karam, O. Boucher, A. Jones, J. E. Kristjánsson, U. Niemeier, M. Schulz, A. Aaheim, F. Benduhn, M. Lawrence, and C. Timmreck (2012), Solar irradiance reduction to counteract radiative forcing from a quadrupling of $CO_2$: climate responses simulated by four earth system models, *Earth System Dynamics*, *3*(1), 63–78.

Scotese, C. R. (2016), *PALEOMAP Project [http://www.scotese.com]*.

Servais, T., A. W. Owen, D. A. Harper, B. Kröger, and A. Munnecke (2010), The Great Ordovician Biodiversification Event (GOBE): the palaeoecological dimension, *Palaeogeography, palaeoclimatology, palaeoecology*, *294*(3), 99–119.

Servais, T., T. Danelian, D. A. T. Harper, and A. Munnecke (2014), Possible oceanic circulation patterns, surface water currents and upwelling zones in the Early Palaeozoic, *GFF*, *136*(1), 229–233.

Sheehan, P. M. (2001), The late Ordovician mass extinction, *Annual Review of Earth and Planetary Sciences*, *29*(1), 331–364.

Steemans, P., A. Le Herissé, J. Melvin, M. A. Miller, F. Paris, J. Verniers, and C. H. Wellman (2009), Origin and radiation of the earliest vascular land plants, *Science*, *324*(5925), 353–353.

Stommel, H. (1961), Thermohaline convection with two stable regimes of flow, *Tellus*, *13*(2), 224–230.

Stouffer, R. J., J. Yin, J. M. Gregory, K. W. Dixon, M. J. Spelman, W. Hurlin, A. J. Weaver, M. Eby, G. M. Flato, H. Hasumi, A. Hu, J. H. Jungclaus, I. V. Kamenkovich, A. Levermann, M. Montoya, S. Murakami, S. Nawrath, A. Oka, W. R. Peltier, D. Y. Robitaille, A. Sokolov, G. Vettoretti, and S. L. Weber (2006), Investigating the causes of the response of the thermohaline circulation to past and future climate changes, *Journal of Climate*, *19*, 1365–1387.

Sutcliffe, O. E., J. A. Dowdeswell, R. J. Whittington, J. N. Theron, and J. Craig (2000), Calibrating the Late Ordovician glaciation and mass extinction by the eccentricity cycles of Earth's orbit, *Geology*, *28*(11), 967–970.

Torsvik, T. H., and L. R. M. Cocks (2009), BugPlates: linking biogeography and palaeogeography, software manual.

Torsvik, T. H., and L. R. M. Cocks (2013), Gondwana from top to base in space and time, *Gondwana Research*, *24*(3-4), 999–1030.

Trabucho-Alexandre, J., W. W. Hay, and P. L. De Boer (2012), Phanerozoic environments of black shale deposition and the Wilson Cycle, *Solid Earth*, *3*(1), 29–42.

Trotter, J. A., I. S. Williams, C. R. Barnes, C. Lécuyer, and R. S. Nicoll (2008), Did cooling oceans trigger Ordovician biodiversification? Evidence from conodont thermometry, *Science*, *321*, 550–554.

Trotter, J. A., I. S. Williams, C. R. Barnes, P. Männik, and A. Simpson (2016), New conodont $\delta^{18}$O records of Silurian climate change: Implications for environmental and biological events, *Palaeogeography, palaeoclimatology, palaeoecology*, *443*(C), 34–48.

Tukey, J. W. (1977), *Exploratory Data Analysis*, Addison-Wesley series in behavioral science, first ed., Addison-Wesley Publishing Company.

Van Cappellen, P., and E. D. Ingall (1994), Benthic phosphorus regeneration, net primary production, and ocean anoxia: A model of the coupled marine biogeochemical cycles of carbon and phosphorus, *Paleoceanography*, *9*(5), 677–692.

Vandenbroucke, T. R. A., P. Emsbo, A. Munnecke, N. Nuns, L. Duponchel, K. Lepot, M. Quijada, F. Paris, T. Servais, and W. Kiessling (2015), Metal-induced malformations in early Palaeozoic plankton are harbingers of mass extinction., *Nature communications*, *6*, 7966.

Vecoli, M., A. Delabroye, A. Spina, and O. Hints (2011), Cryptospore assemblages from Upper Ordovician (Katian–Hirnantian) strata of Anticosti Island, Québec, Canada, and Estonia: Palaeophytogeographic and palaeoclimatic implications, *Review of Palaeobotany and Palynology*, *166*, 76–93.

Walker, L. J., B. H. Wilkinson, and L. C. Ivany (2002), Continental drift and Phanerozoic carbonate accumulation in shallow-shelf and deep-marine settings, *The Journal of geology*, *110*(1), 75–87.

Wallmann, K. (2003), Feedbacks between oceanic redox states and marine productivity: A model perspective focused on benthic phosphorus cycling, *Global Biogeochemical Cycles*, *17*(3), 1084.

Webby, B. D., F. Paris, M. L. Droser, and I. G. Percival (Eds.) (2004), *The Great Ordovician Biodiversification Event*, Critical moments and perspectives in Earth history and paleobiology, Columbia University Press, New York.

Winton, M. (2000), A reformulated three-layer sea ice model, *Journal of Atmospheric and Oceanic Technology*, *17*(4), 525–531.

Yamanaka, Y., and E. Tajika (1997), Role of dissolved organic matter in the marine biogeochemical cycle: Studies using an ocean biogeochemical general circulation model, *Global Biogeochemical Cycles*, *11*(4), 599–612.

Yan, D., D. Chen, Q. Wang, J. Wang, and Z. Wang (2009), Carbon and sulfur isotopic anomalies across the Ordovician–Silurian boundary on the Yangtze Platform, South China, *Palaeogeography, palaeoclimatology, palaeoecology*, *274*(1-2), 32–39.

Young, S. A., M. R. Saltzman, W. I. Ausich, A. Desrochers, and D. Kaljo (2010), Did changes in atmospheric $CO_2$ coincide with latest Ordovician glacial–interglacial cycles?, *Palaeogeography, palaeoclimatology, palaeoecology*, *296*(3-4), 376–388.

Zhang, T., Y. Shen, R. Zhan, S. Shen, and X. Chen (2009), Large perturbations of the carbon and sulfur cycle associated with the Late Ordovician mass extinction in South China, *Geology*, *37*(4), 299–302.

Zhou, L., P. B. Wignall, J. Su, Q. Feng, S. Xie, L. Zhao, and J. Huang (2012), U/Mo ratios and $\delta^{98/95}$Mo as local and global redox proxies during mass extinction events, *Chemical Geology*, *324-325*(C), 99–107.

Zhuravlev, A. Y., and R. Riding (2001), *The ecology of the Cambrian radiation*, Critical moments in paleobiology and earth history, Columbia University Press, New York.